ORIGINAL

Michele De Angelo · Emilio Barchiesi · Ivan Giorgio ·
B. Emek Abali

Numerical identification of constitutive parameters in reduced-order bi-dimensional models for pantographic structures: application to out-of-plane buckling

Abstract Mechanical properties are investigated for a class of microstructured materials with promising applications. Specifically, we consider a composite material with orthogonal, mutually interconnected fibers building a pantographic substructure. In order to predict the behavior of such a system in three-dimensional continuum, a reduced-order model is introduced by means of a bi-dimensional elastic surface accurately describing large deformations. The properties of this reduced-order model are characterized by an elastic energy density that involves second space derivatives of the displacement for capturing the resistance of twisted and bent fibers in plane as well as out of plane. For determining the coefficients in the elastic energy of the reduced-order model, we utilize a numerical inverse analysis and make use of ad hoc computational experiments performed by a direct numerical simulation on the microscale with detailed modeling of the pantographic substructure. This reduced-order model represents a homogenized material on macro-scale with its substructure on microscale. The homogenized model is capable of describing materials response at a significantly less computational cost than the direct numerical simulations.

1 Introduction

In this work, we determine coefficients in a homogenized material with a pantographic substructure. This homogenized material is commonly called a *metamaterial*, as it exhibits an 'exotic' behavior due to its peculiar microstructure: in-plane bending of its constituting fibers gives rise at macroscopic scale to so-called second gradient effects which are not typical of materials customarily used in engineering practice [14,22,30,52,55]. Such a microstructure consists, in the reference configuration, of a double array of orthogonal beams (also called fibers) which are interconnected by cylinders, also called pivots, at their intersection points [26–28] (see Figs. 1, 2). The latter structural elements resemble a rotational/torsional elastic stiffness that restricts the relative rotation of fibers. This particular microstructure results in a compliant material, which can undergo large deformations in elastic regime exhibiting a characteristic stiffening behavior. In order to describe the mechanical behavior of

M. De Angelo · I. Giorgio (✉)
International Research Center for the Mathematics and Mechanics of Complex Systems, Università dell'Aquila, 67100 L'Aquila, Italy
E-mail: ivan.giorgio@uniroma1.it

I. Giorgio · E. Barchiesi
Department of Structural and Geotechnical Engineering, Università di Roma La Sapienza, 18 Via Eudossiana, 00184 Rome, Italy

B. Emek Abali
Chair of Continuum Mechanics and Constitutive Theory, Institute of Mechanics, Technische Universität Berlin, Einsteinufer 5, 10587 Berlin, Germany
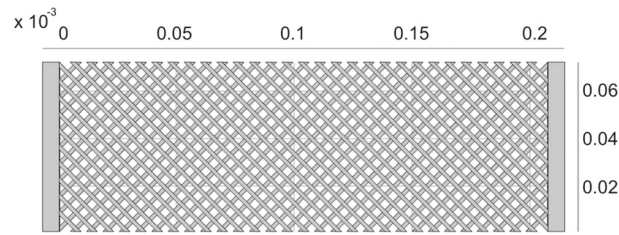
Fig. 1 Top view of the pantographic structure

such a system, many reduced-order models have been proposed in the recent literature for inextensible fibers [20,23,25,46,61], systems with relative displacements in their microstructure [44,72,77], for nonorthogonal fibers and/or curved fibers prior the deformation [40,69,76,78], employing discrete [18,74,75], semi-discrete [10,24,48], or continuum models [5,15,42,65,70,71,73]. All continuum models share the same mathematical feature: the homogenized deformation energy depends not only on the first gradient but also on the second gradient of the displacement [62,63] in order to account for in-plane bending of fibers [4,13,59]. So far, the experimental and numerical evidences gathered in the literature concern to a greater extent specimens deforming in plane. The particular substructure of such a metamaterial is very similar to that of the woven structures, textile materials, and lattice truss materials; therefore, the models describing them are very similar (see, e.g., [11,19,33,37,64]). Besides, the homogenization techniques used for micropolar and textile materials can be usefully adopted for the considered structure (see for some hints [17,21,31,32,34,35,43,66,68]).

The present work considers the homogenized model as proposed in [42], where the composite material is a plate modeled by 2D continuum embedded in 3D space. This so-called reduced-order model characterizes the deformation accurately by using parameters in the homogenized material model. In order to determine these parameters, we perform an inverse analysis by exploiting a set of numerical experiments obtained by a direct numerical simulation using the Cauchy continuum with a detailed model of the pantographic substructure since in the smallest length scale the Cauchy continuum is accurate [53]. For the inverse analysis, we employ the nonlinear regression method minimizing the error known as the least squares method. Additionally, we make use of different numerical experiments in order to examine and validate the numerical values of parameters obtained by the inverse analysis. We emphasize that, in particular, we have been able to numerically reproduce the onset of buckling modes by using the direct numerical simulation as well as reduced-order model representing the homogenized material—these buckling modes are experimentally observed in [12].

Since the reduced model, considered herein, is characterized by second displacement gradients in the energy, the process of identification is performed carefully by taking into account the mathematical consistency; for some useful hints about such issues, we refer to [3,6–8,36,50,56,58,65]).

The plan of the work is as follows. In Sect. 2, we present the continuum models employed for the identification. Specifically, the homogenized reduced-order model is thoroughly described in Sect. 2.1, while the Cauchy micro-model is presented in Sect. 2.2. In Sect. 3, we present the inverse analysis for determining the coefficients in the homogenized model. In particular, we describe the setup of the numerical experiments involved in the inverse analysis. In this section, furthermore, the definitions of the defined least squares objective functions are given. In Sect. 4, we show that the parameters obtained by the previous identification allow us to match closely the results of the two models also for further numerical tests. Finally, we present a sensitivity study in Appendix A, which consists in evaluating the change in the results of the macro-model by varying the constitutive stiffnesses in a neighborhood of the identified stiffness set.

2 Pantographic structure and modeling

We introduce a general approach for constructing a reduced-order model and determination of parameters. In order to present this approach concretely, we specify a particular case of a metamaterial with pantographic substructure as shown in Fig. 2. The shape of the specimen and the coefficients generating the substructure are compiled in Table 1. Particularly, they are: (1) the dimensions of the fiber cross sections, i.e., b_b and h_b; the diameter and the height of the pivots, i.e., d_p and h_p, respectively; the overall sizes of the sample, i.e., L and l; the angle between fibers prior to deformation, i.e., ϑ^*; and the pitch between the fibers belonging to the same array, i.e., p. For example in [79], the same pantographic substructure is built out of polyamide and physically tested. The approximate properties of this material are presented in Table 2.
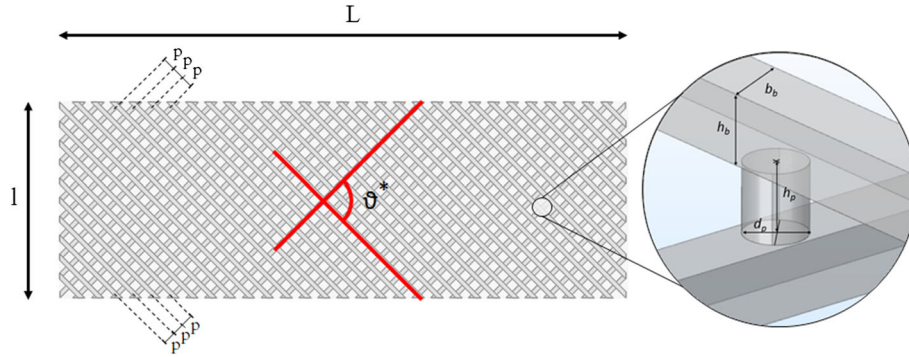
Fig. 2 Geometric features of the specimen

Table 1 Fibers and pivot dimensions in mm (millimeter), angle in rad (radian)

b_b	h_b	d_p	h_p	L	l	ϑ^*	p
1.60	1.00	0.9	1.00	210	70	$\pi/2$	4.85

In what follows, we provide a concise description of the two models adopted for the inverse analysis: the homogenized model presented in [42] provides a macro-description of the considered structure at a lower computational cost; therefore, we refer to it as macro-model, and the Cauchy continuum model, which accurately describes the deformation by modeling the substructure in full detail at a very high numerical cost [39]; we refer to it as micro-model (or reference model).

2.1 2D continuum model

Regarding the geometric dimensions of the specimen, we consider it as a plate. In order to describe the deformation of a pantographic plate, several studies in the literature use a two-dimensional model [9,26,29, 59,60]. Most of these studies can be subsumed under the assumption of in-plane deformation. In this paper, we carry out an identification of the constitutive parameters for a recently proposed second gradient, orthotropic 2D reduced model, allowing to analyze problems that involve large deformations and out-of-plane displacements.

Let us consider a rectangular 2D continuum embedded in the 3D Eulerian space and equipped with a continuous planar fibers' square grid formed by the intersection of two orthogonal families of beams. In other words, the discrete microstructure of beams (fibers) described in [42] is homogeneously distributed in the considered region of the space. A rectangular domain is the reference configuration $\mathfrak{R} \subset \mathbb{R}^2$ of the pantographic plate. A global Cartesian coordinate system is introduced, being the orthonormal basis the triple $(\mathbf{D}_1, \mathbf{D}_2, \mathbf{D}_3 = \mathbf{D}_1 \times \mathbf{D}_2)$, with $\mathbf{D}_1$ and $\mathbf{D}_2$ parallel to the two fiber families. At each point of this region, two rigid planes moving in the space are considered. They are, respectively, orthogonal to one of the fibers intersecting in that point and stand for the fibers' cross section. In the reference configuration, a point $X \in \mathfrak{R}$ can be represented by means of the coordinates (X_1, X_2), while the orientation of the corresponding attached rigid planes is given by means of the vectors:

- $^\alpha\mathbf{E}$ which is the unit vector orthogonal to the cross section, with $\alpha = 1, 2$ indexing the two families of fibers (α stands for the family of fibers parallel to $\mathbf{D}_\alpha$);
- $\mathbf{N} =^1 \mathbf{E} \times^2 \mathbf{E}$;
- $^\alpha\mathbf{M} = \mathbf{N} \times^\alpha \mathbf{E}$.

For the sake of clarity, the case $\mathbf{D}_\alpha = {}^\alpha\mathbf{E}$ corresponds to fibers of 'Euler–Bernoulli-type,' where the cross sections remain orthogonal to the fibers' lines. Referring to Fig. 3, we assume that in the reference configuration (a) $^1\mathbf{E}$ and $^1\mathbf{M}$ coincide with $\mathbf{D}_1$ and $\mathbf{D}_2$, respectively, (b) $^2\mathbf{E}$ and $^2\mathbf{M}$ coincide with $-\mathbf{D}_2$ and $\mathbf{D}_1$, respectively, (c) $\mathbf{N} = \mathbf{D}_3$. Besides, we assume that $^\alpha\mathbf{M}$ and $\mathbf{N}$ are directed along the principal axes of the beam cross sections. A deformed configuration is characterized by a placement

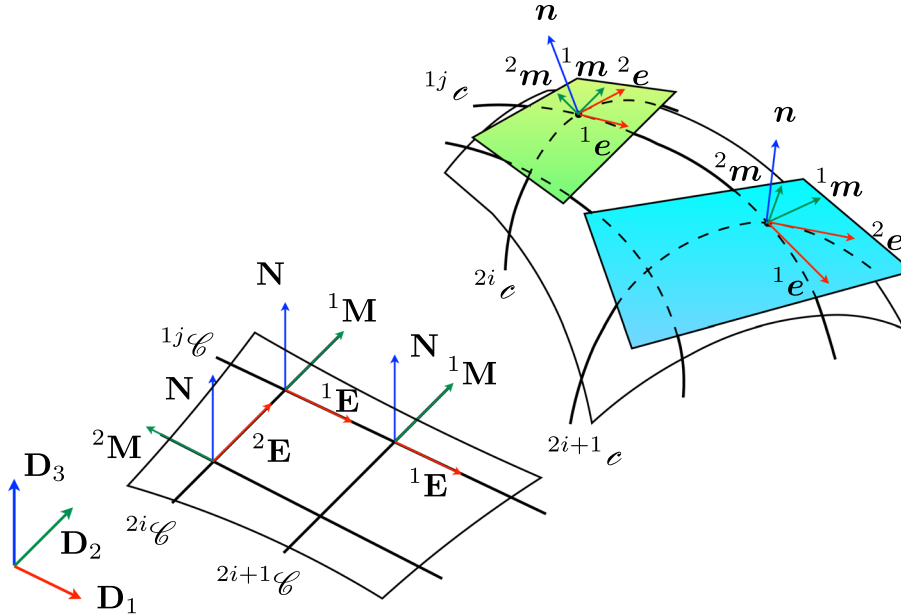| Mechanical property	Value
Mass density (ϱ)	0.93 g cm^{-3}
Young's modulus (E)	1600 N mm^{-2}
Poisson's ratio (ν)	0.3

Fig. 3 Microstructure in the bi-dimensional model, where the network of the fibers is highlighted in the reference and in the current configuration

$$\chi : \mathfrak{R} \to \mathfrak{S}$$
$$X \mapsto x = \chi(X), \tag{1}$$

where $\mathfrak{S} \subset \mathbb{R}^3$ is the representation of the current surface, and two orthogonal tensor fields

$$^1\boldsymbol{R} : \quad (\mathbf{D}_1, \mathbf{D}_2, \mathbf{D}_3) \mapsto (^1\boldsymbol{a}_1, {}^1\boldsymbol{a}_2, {}^1\boldsymbol{a}_3) \tag{2}$$
$$^2\boldsymbol{R} : \quad (\mathbf{D}_1, \mathbf{D}_2, \mathbf{D}_3) \mapsto (^2\boldsymbol{a}_1, {}^2\boldsymbol{a}_2, {}^2\boldsymbol{a}_3) \tag{3}$$

where $(^1\boldsymbol{a}_1, {}^1\boldsymbol{a}_2, {}^1\boldsymbol{a}_3)$ and $(^2\boldsymbol{a}_1, {}^2\boldsymbol{a}_2, {}^2\boldsymbol{a}_3)$ give the orientation of the microstructure in the deformed configuration as an effect of the rotations $^1\boldsymbol{R}$ and $^2\boldsymbol{R}$. Finally, we define the displacement field as

$$\boldsymbol{u}(X) = x - X = u_1(X)\mathbf{D}_1 + u_2(X)\mathbf{D}_2 + u_3(X)\mathbf{D}_3. \tag{4}$$

We denote the vectors tangent to the deformed coordinate lines by

$$^\alpha\boldsymbol{t} = \frac{\partial \chi}{\partial X_\alpha} \quad \alpha = 1, 2 , \tag{5}$$

as well as their corresponding normalized tangent vectors,

$$^\alpha\boldsymbol{e} = \frac{^\alpha\boldsymbol{t}}{\|^\alpha\boldsymbol{t}\|} , \tag{6}$$

whereas they are straight in the reference configuration. Moreover, we denote the unit normal to the deformed surface by

$$\boldsymbol{n} = \frac{{}^1\boldsymbol{e} \times {}^2\boldsymbol{e}}{\|{}^1\boldsymbol{e} \times {}^2\boldsymbol{e}\|} \tag{7}$$

and

$$\,{}^\alpha \boldsymbol{m} = \boldsymbol{n} \times {}^\alpha \boldsymbol{e} \tag{8}$$

We enforce the following constrains at each point $X \in \mathfrak{R}$:

C1: ${}^1\boldsymbol{a}_1 = {}^1\boldsymbol{e}$ and ${}^2\boldsymbol{a}_1 = {}^2\boldsymbol{e}$
C2: ${}^1\boldsymbol{a}_3 = {}^2\boldsymbol{a}_3 = \boldsymbol{n}$
C3: ${}^1\boldsymbol{a}_2 = {}^1\boldsymbol{m}$ and ${}^2\boldsymbol{a}_2 = {}^2\boldsymbol{m}$

As a consequence of these constraints, the rotations ${}^1\boldsymbol{R}$ and ${}^2\boldsymbol{R}$, and therefore the orientation of the two rigid planes representing the local microstructure, are completely determined by the current shape of the corresponding coordinate lines passing through the point X. As a result, the beams are assumed to be without shear deformation (**C1**). Therefore, the two rotations ${}^1\boldsymbol{R}$ and ${}^2\boldsymbol{R}$ can be related to the gradient of the displacement. However, *a priori* the two bases of the cylindrical pivots can rotate independently. Hence, in the kinematic description we need two distinct rotations ${}^1\boldsymbol{R}$ and ${}^2\boldsymbol{R}$. We further assume a remarkable constraint on ${}^1\boldsymbol{R}$ and ${}^2\boldsymbol{R}$ (**C2**). Indeed, for each point $X \in \mathfrak{R}$, we have, in the current configuration, that the normal vectors to the concurring fibers do coincide. Moreover, having two different rotations ${}^1\boldsymbol{R}$ and ${}^2\boldsymbol{R}$ allows to take into account torsion of cylindrical pivots, i.e., macroscopic shear deformations as well as torsion of fibers embedded in the considered elastic surface.

Using the notation above, it becomes possible to define the local deformation measures for the 2D continuum as

$$\,{}^\alpha \varepsilon = \|{}^\alpha \boldsymbol{t}\| - 1, \quad {}^1\boldsymbol{e} \cdot {}^2\boldsymbol{e} = \sin(\gamma) \tag{9}$$

${}^\alpha \varepsilon$ being the local elongation and γ the shear angle, and[1]

$$\,{}^\alpha \boldsymbol{W} = {}^\alpha \boldsymbol{R}^\top \frac{\partial^\alpha \boldsymbol{R}}{\partial X_\alpha} = {}^\alpha \kappa_1 \mathbf{D}_2 \wedge \mathbf{D}_3 + {}^\alpha \kappa_2 \mathbf{D}_3 \wedge \mathbf{D}_1 + {}^\alpha \kappa_3 \mathbf{D}_1 \wedge \mathbf{D}_2 \quad \text{(no sum over } \alpha) \tag{10}$$

where ${}^\alpha \boldsymbol{W}$ is the second-order curvature tensor, which is a skew tensor, and ${}^\alpha \kappa_1$, ${}^\alpha \kappa_2$ and ${}^\alpha \kappa_3$ are the components of the corresponding axial vector.

The strain measures, expressed in terms of the displacement components, turn out to be

$$\,{}^1\kappa_1 = \frac{\boldsymbol{n} \cdot \boldsymbol{g}_1 - \sin(\gamma)\,\boldsymbol{n} \cdot \boldsymbol{c}_1}{\|{}^1\boldsymbol{e} \times {}^2\boldsymbol{e}\|}, \quad {}^1\kappa_2 = \boldsymbol{n} \cdot \boldsymbol{c}_1, \quad {}^1\kappa_3 = -{}^1\boldsymbol{m} \cdot \boldsymbol{c}_1 \tag{11}$$

$$\,{}^2\kappa_1 = \frac{\boldsymbol{n} \cdot \boldsymbol{g}_2 - \sin(\gamma)\,\boldsymbol{n} \cdot \boldsymbol{c}_2}{\|{}^1\boldsymbol{e} \times {}^2\boldsymbol{e}\|}, \quad {}^2\kappa_2 = \boldsymbol{n} \cdot \boldsymbol{c}_2, \quad {}^2\kappa_3 = -{}^2\boldsymbol{m} \cdot \boldsymbol{c}_2 \tag{12}$$

where the variables $\boldsymbol{c}_1, \boldsymbol{c}_2, \boldsymbol{g}_1, \boldsymbol{g}_2$ are defined as follows:

$$\boldsymbol{c}_1 = \frac{(\nabla\nabla\chi)\mathbf{D}_1 \otimes \mathbf{D}_1}{\|\nabla\chi\,\mathbf{D}_1\|} \quad \boldsymbol{c}_2 = \frac{(\nabla\nabla\chi)\mathbf{D}_2 \otimes \mathbf{D}_2}{\|\nabla\chi\,\mathbf{D}_2\|}$$

$$\boldsymbol{g}_1 = \frac{(\nabla\nabla\chi)\mathbf{D}_2 \otimes \mathbf{D}_1}{\|\nabla\chi\,\mathbf{D}_2\|} \quad \boldsymbol{g}_2 = \frac{(\nabla\nabla\chi)\mathbf{D}_1 \otimes \mathbf{D}_2}{\|\nabla\chi\,\mathbf{D}_1\|}.$$

In view of the assumed constraints, we note that ${}^\alpha \kappa_1$, ${}^\alpha \kappa_2$ and ${}^\alpha \kappa_3$ are the geodesic torsion, the normal curvature and the geodesic curvature multiplied by $\|{}^\alpha \boldsymbol{t}\|$, respectively.

The following strain energy density is assumed

$$W = \frac{1}{2}\Big[K_e\big({}^1\varepsilon^2 + {}^2\varepsilon^2\big) + K_s\gamma^2 + K_t\big({}^1\kappa_1^2 + {}^2\kappa_1^2\big) + K_n\big({}^1\kappa_2^2 + {}^2\kappa_2^2\big) + K_g\big({}^1\kappa_3^2 + {}^2\kappa_3^2\big)\Big] \tag{13}$$

---

[1] We use the wedge product, $\wedge$, defined as, $(\boldsymbol{u} \wedge \boldsymbol{v})_{ij} = u_i v_j - v_i u_j$. Therefore, we have $\mathbf{D}_i \wedge \mathbf{D}_j = \mathbf{D}_i \otimes \mathbf{D}_j - \mathbf{D}_j \otimes \mathbf{D}_i$, where $\otimes$ is the usual tensor (dyadic) product.

where K_e, K_t, K_n and K_g are positive constitutive parameters representing the stiffnesses related to the elongation, twist, normal and geodesic bending, respectively. Finally, K_s is the shear stiffness between beams belonging to the two different families. We note that in the above choice of the energy the same constitutive parameters have been selected for both two families of beams. We remark that the numerical study of higher gradient continuum models requires some nontrivial improvements in the standard methods. We emphasize the additional effort for a computational study as conducted for example in [45,51,54,57]. Because of the nature of Eq. (13), which involves the second gradient of the independent displacement field $\boldsymbol{u}$, the considered second-grade elastic surface is also able to sustain double forces and corner forces. Moving forward, for the sake of simplicity, we impose only geometric boundary conditions.

2.2 Cauchy continuum model

We want to determine the numerical values of K_e, K_s, K_n, K_g and K_t in Eq. (13) by using a set of numerical experiments. In the following, we 'construct' computational experiments by using a direct numerical simulation. In other words, we utilize Cauchy continuum on the microscale and perform a simulation with the detailed substructure. St. Venant–Kirchhoff material model is employed in order to accurately capture the large deformation. The energy is quadratic in the Green–Lagrange strain tensor. We emphasize that geometric nonlinearities are of importance to capture accurately such that the choice of St. Venant–Kirchhoff material model is justified. Moreover, it is very convenient to use it when compared with the corresponding model in 2D as given in Eq. (13); both are equally nonlinear in deformation fields. Depending on the chosen material, on top of the geometric nonlinearities, it might be even necessary to consider the material nonlinearities as well; for an experimental study of such effects, we refer to [79]. We restrict our study to the geometrically nonlinear case.

Let us consider a body which occupies a region $\mathfrak{B} \subset \mathbb{R}^3$ of the three-dimensional Euclidean space. This region is referred to as reference configuration, and the location of each material point P of the body is denoted by its material coordinates $\boldsymbol{X}$. The current position of P is described by a suitably regular map $\chi : \mathbb{R}^3 \longrightarrow \mathbb{R}^3$, and it is denoted by $\boldsymbol{x} = \chi(\boldsymbol{X})$. By using the conventional continuum mechanical notation, we introduce the deformation gradient tensor $\boldsymbol{F} = \nabla\chi$ and the Green–Lagrange strain tensor:

$$\boldsymbol{E} = \frac{1}{2}(\boldsymbol{F}^\top \boldsymbol{F} - \boldsymbol{I}). \tag{14}$$

By introducing the displacement

$$\boldsymbol{u}(\boldsymbol{X}) = \chi(\boldsymbol{X}) - \boldsymbol{X}, \tag{15}$$

we recast (14) as

$$\boldsymbol{E}(\boldsymbol{X}) = \frac{1}{2}(\nabla\boldsymbol{u} + \nabla\boldsymbol{u}^\top + \nabla\boldsymbol{u}^\top\nabla\boldsymbol{u}). \tag{16}$$

Assuming the constitutive relation for isotropic and homogeneous materials, the strain energy density is defined as

$$W_\mathrm{V}(\boldsymbol{E}) = \frac{\lambda}{2}[\mathrm{tr}(\boldsymbol{E})]^2 + \mu\,\mathrm{tr}(\boldsymbol{E}^2). \tag{17}$$

where λ and μ are the Lamé parameters. We remark that the material constituting the structure at micro-level, polyamide, is assumed to be isotropic, while the orthogonal arrangement of fibers implies at macro-level an orthotropic material symmetry group. The governing equations are stated by means of a variational principle as follows

$$\delta \int_\mathfrak{B} W_\mathrm{V}(\boldsymbol{E})\mathrm{d}V = 0, \quad \forall\,\delta\boldsymbol{u}$$

with $\delta\boldsymbol{u}$ being kinematically admissible variations in the displacement field [1,2]. As concern the boundary conditions, in what follows, we assign displacements on a proper subset of the surface accordingly with the considered case.
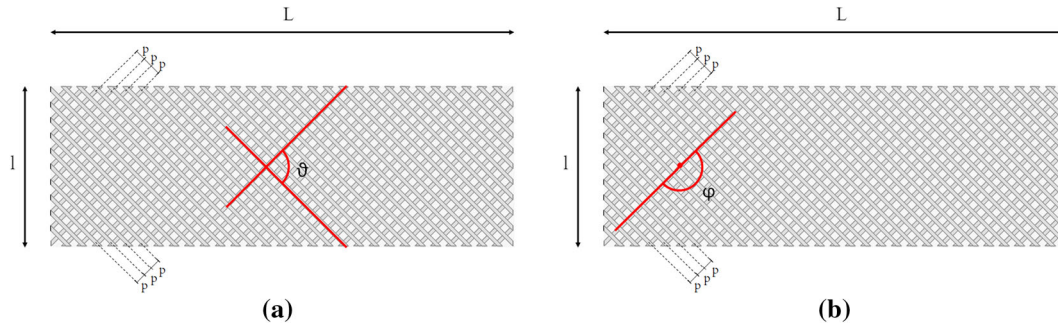
Fig. 4 Angles θ and ϕ in one location

3 Inverse analysis

In this section, we aim at determining the numerical values of coefficients arising in the homogenized model on the macro-scale effected by the substructure on the microscale. The approach is based on the idea explained in [26]. Simply stated, we use numerical experiments on microscale and obtain the parameters, K_e, K_s, K_n, K_g and K_t in Eq. (13), in order to characterize the homogenized model. The proposed approach to determine the aforementioned parameters of the pantographic plate is based on direct numerical simulations of two experiments. The key idea, here, consists in designing these two numerical experiments in order to control, which deformation measure is being 'activated,' see [41,47,49,58]. As the first numerical experiment, we consider a bias extension test, which is characterized by an in-plane deformation. This test activates only fibers' extension, in-plane bending and shear; thus, the corresponding stiffnesses, K_e, K_g and K_s, become relevant. By using the results of the numerical experiments, these parameters are determined by an inverse analysis. The remaining parameters, K_n and K_t, are simply not involved in this test; hence, we just estimate their values as in [42,72] and obtain their values by using the second numerical experiment. As the second numerical experiment, we design an out-of-plane bias shear test in order to make the remaining parameters, K_n and K_t, relevant. In this deformation mode associated with fibers' extension, in-plane bending and shear are negligible and out-of-plane bending and twist become dominant.

Specifically, the first experiment is the in-plane bias extension test designed to determine K_e, K_g and K_s. Such a test is usually employed to characterize the in-plane behavior of a woven fabric—the structure of a woven fabric with threads at right angles is equivalent to the pantographic structure studied herein. The numerical experiment is conducted on the specimen as shown in Fig. 2 by clamping the left side and stretching the right side under a prescribed elongation up to 6 cm in several loading steps, to attain a large strain regime. In each loading step, the total energy, $\mathscr{E}^m$, and two different angles, θ^m and ϕ^m, as shown in Fig. 4 are computed by using the micro-model with the parameters from Table 2. In particular, θ^m is evaluated at the center of the sample. We remark that this angle is a global quantifier because it is constant in all the central zone (apart from border effects), as it is well known in the case of woven fabric (see *A* zone in Fig. 7 in [48]). The angle ϕ^m is evaluated at the vertex of the almost rigid triangle near the short edge (see *C* zone in Fig. 7 in [48]). Similarly, it characterizes the boundary layer which surrounds the above-mentioned triangle due to the in-plane bending of the fibers. In each loading step, their values are recorded and denoted by $\mathscr{E}_i^m$, θ_i^m, ϕ_i^m. We generate in such a way the experimental data by using the direct numerical simulations. In the case of the homogenized model, by using some parameters for K_e, K_g and K_s, we compute the total energy and angles, this time for the macro-model, $\mathscr{E}_i^M$, θ_i^M, ϕ_i^M. For the best values of K_e, K_g, K_s, the differences between the corresponding values would be minimal. Hence, we aim at finding the parameters, minimizing the following object function:

$$f = \sum_i^n \left(\frac{\mathscr{E}_i^M - \mathscr{E}_i^m}{\mathscr{E}_i^m} \right)^2 + \sum_i^n \left(\frac{\vartheta_i^M - \vartheta_i^m}{\vartheta_i^m} \right)^2 + \sum_i^n \left(\frac{\varphi_i^M - \varphi_i^m}{\varphi_i^m} \right)^2 \qquad (18)$$

where

- i is the index of the i-th step loading;
- quantities denoted by M are obtained from the macroscopic model;
- quantities with m are computed by the microscopic model.

We remark that the objective function has been normalized to equally weigh up each of the error contribution from different physical variables. This optimization problem is a nonlinear regression such that the initial guess of parameters becomes essential. We start off with an initial guess for the parameters as compiled in Table 3 by using the ideas from [16,42,59,67,72]. With these initial values, we determine the three stiffnesses, K_e, K_g and K_s, successfully as shown in Fig. 5 the energy density distribution as colors and the deformation without scaling for micro-model (top) and macro-model (below). As a first trial, we have chosen all values listed in Table 3. There, E and G are the Young and the shear modulus, respectively, A is the area of the fibers' cross sections, and I_z, I_y and J_t are the flexural, in plane and out of plane, as well as the torsional second moment of area of the beams' cross sections, respectively. As in [26], we correlate the angle θ (see Fig. 4a) to K_s and the angle ϕ (see Fig. 4b) to K_b and use, as a further quantifier, the total amount of strain energy, $\mathscr{E}$, in the deformation process to determine K_e.

After having determined the first three stiffnesses, we proceeded by conducting the second numerical experiment for determining K_n and K_t. The so-called out-of-plane bias shear test prescribes an imposed uniform displacement to the short right side up to 7 cm along the out-of-plane direction, which preserves its length, while the left short side was fixed. Furthermore, in order to prevent the occurrence of (undesirable, as they activate energy terms which have been considered in the in-plane bias extension test and would, therefore, shade the other energy terms related to the stiffnesses which we want to fit in the out-of-plane bias shear test)

Table 3 Initial guess for the nonlinear regression problem

K_e	K_g	K_n	K_t	K_s
$\dfrac{E\,A}{p}$	$\dfrac{E\,I_z}{p}$	$\dfrac{E\,I_y}{p}$	$\dfrac{G\,J_t}{p}$	$\dfrac{G\,\pi\,d_p^4}{32\,h_p\,p^2}$

(a) 3D Cauchy model.
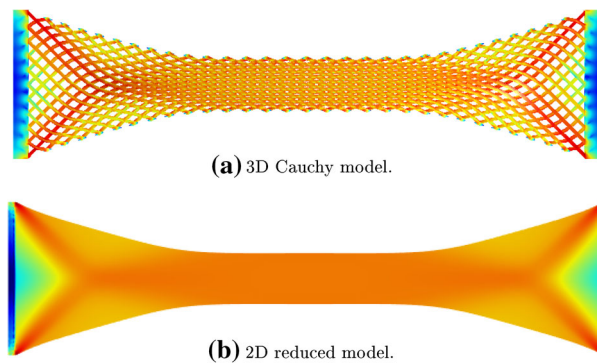

(b) 2D reduced model.

Fig. 5 In-plane bias extension test scheme, the colors indicate strain energy density, and the deformation is presented without scaling. Top: results obtained from the numerical experiment. Below: results delivered by the reduced-order model
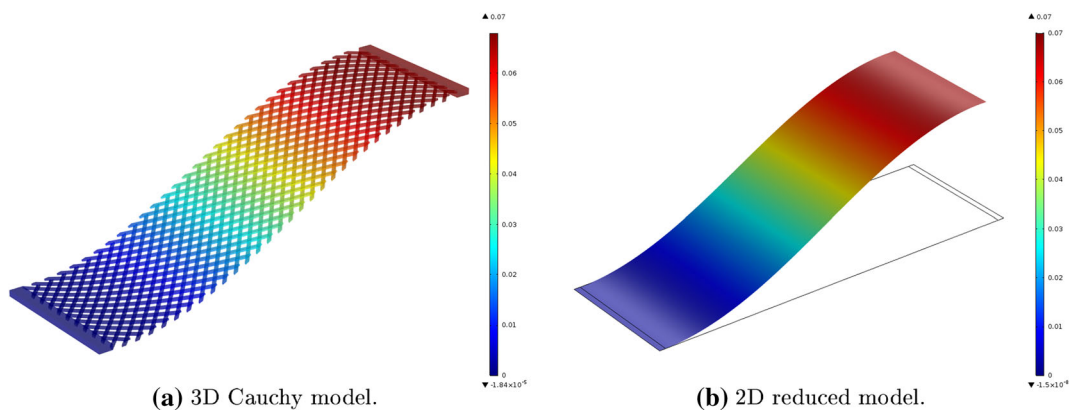

(a) 3D Cauchy model. **(b)** 2D reduced model.

Fig. 6 Deformed shapes (micro-model and macro-model) for out-of-plane bias shear test. The legend refers to the out-of-plane displacement, u_3
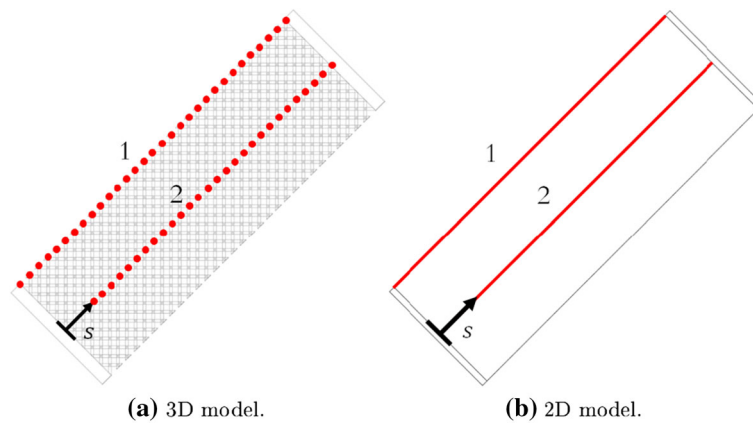
(a) 3D model.   **(b)** 2D model.

Fig. 7 Probe points (left) and probe lines (right) for evaluating the deformed shape and the out-of-plane displacement w_{ij}

(a) strain energy

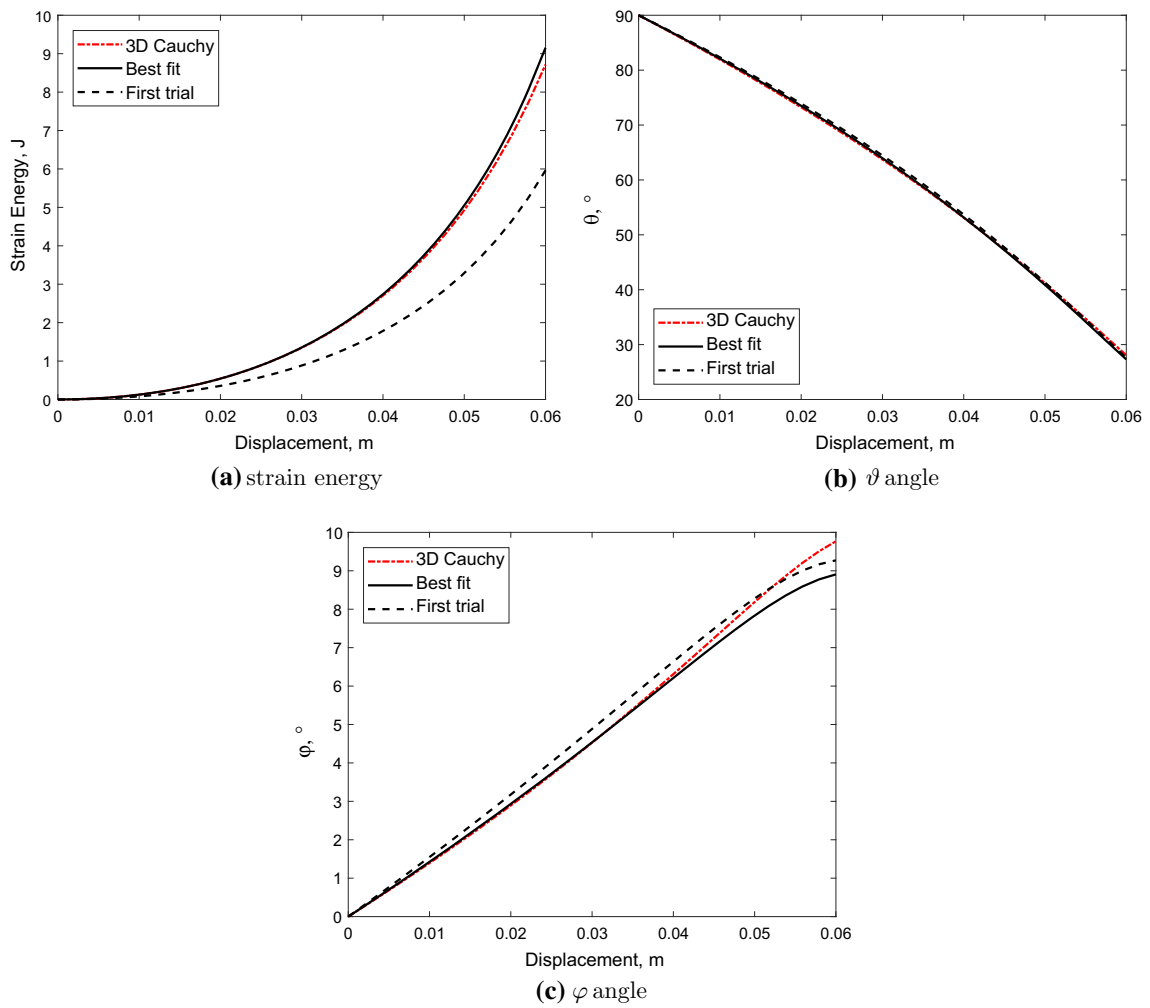**(b)** ϑ angle

(c) φ angle

Fig. 8 Comparison between 2D first trial, 2D best fit and 3D Cauchy model for plane bias extension test

extensional deformations, all the rotations of the right short side are prevented (in the micro-model this means that the handle in correspondence of the short side cannot rotate, in the macro-model $^1R = {}^2R = I$ at the same edge), while the displacement along the longitudinal direction is free, being imposed to zero the component of the displacement parallel to the same side. Figure 6 shows a deformed shape produced by the shear test.

In order to verify that the two experiments effectively decouple the stiffnesses, we performed sensitivity analyses and successfully checked that the objective functions are weakly dependent on the parameters related to deformations which are not to be activated. The absence of the rotations of the short displaced side guarantees this condition, as will be shown below.

Analogous to the previous case, quantities are chosen to carry out the identification. In detail, we take into consideration the total strain energy, $\mathscr{E}$, and the out-of-plane displacement, w, (since extension, i.e., axial displacement, is avoided effected by the imposed boundary conditions) of the longitudinal axis of the specimen. With regard to this last quantity, the micro–macro-comparison is achieved by calculating the vertical displacement of the 3D point array number 2 indicated in Fig. 7a, w_{ij}^m, and the corresponding points of the curve number 2 in Fig. 7b, w_{ij}^M. Also in this case, a nondimensional least squares objective function has been built and it has the following expression:

$$ f = \sum_i^n \left(\frac{\mathscr{E}_i^M - \mathscr{E}_i^m}{\mathscr{E}_i^m} \right)^2 + \frac{1}{N_p} \sum_i^n \sum_j^{N_p} \left(\frac{w_{ij}^M - w_{ij}^m}{w_{ij}^m} \right)^2 \tag{19} $$

Table 4 Stiffnesses identified with in-plane bias extension test identification

K_e	K_g	K_n	K_t	K_s
$1.5 \frac{EA}{p}$	$2.1 \frac{E I_z}{p}$	$\frac{E I_y}{p}$	$\frac{G J_t}{p}$	$1.5 \frac{G \pi d_p^4}{32 h_p p^2}$

Table 5 Best stiffness set

K_e	K_g	K_n	K_t	K_s
$1.5 \frac{EA}{p}$	$2.1 \frac{E I_z}{p}$	$0.5 \frac{E I_y}{p}$	$1 \frac{G J_t}{p}$	$1.5 \frac{G \pi d_p^4}{32 h_p p^2}$

(a) Contributions to strain energy

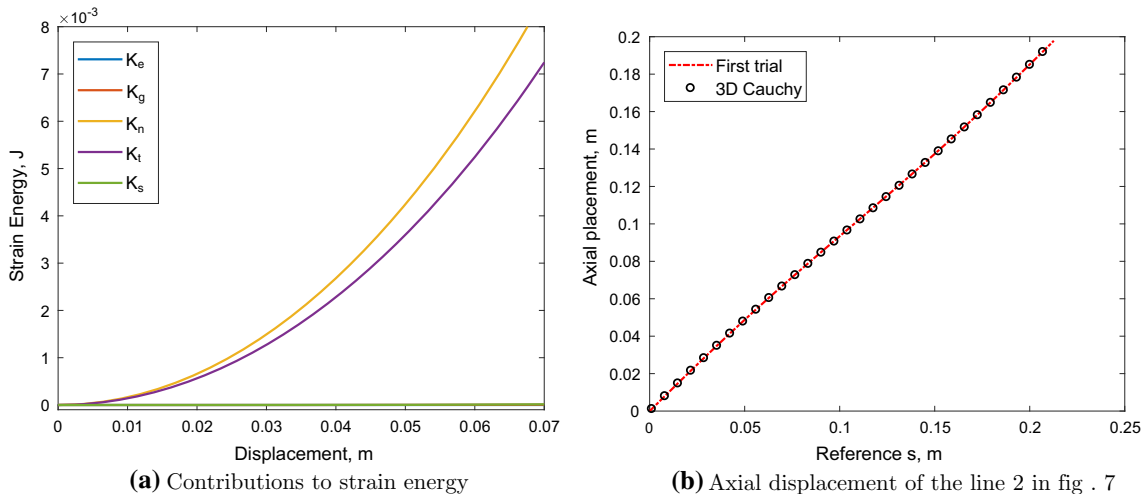**(b)** Axial displacement of the line 2 in fig . 7

Fig. 9 Out-of-plane bias shear test, verification of independence from plane bias test

where

- M and m are the apexes which indicate that the considered quantity is related to the macroscopic and microscopic model, respectively;
- i is the index of the i-th step loading;
- j is the index of the j-th evaluation point;
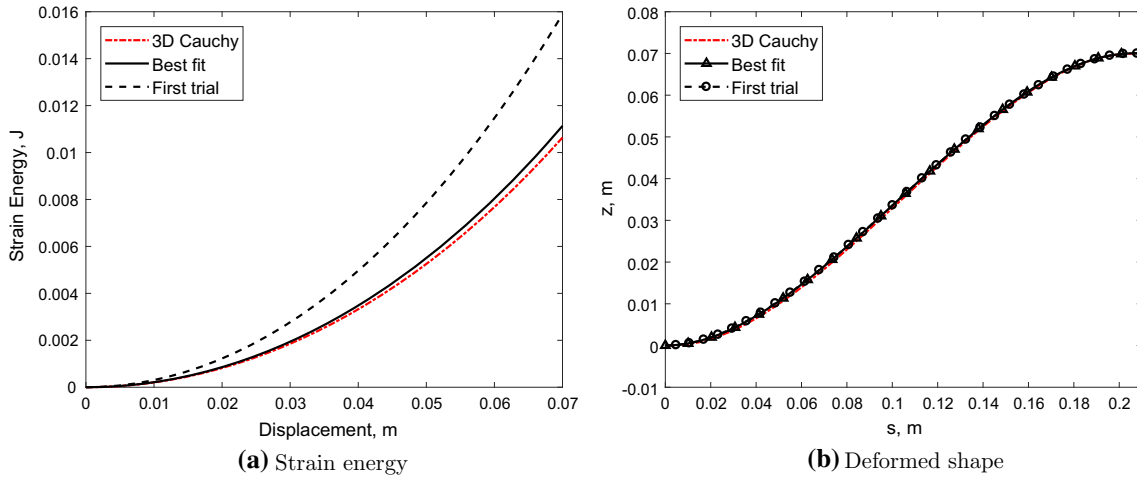- N_p number of the evaluating points.

(a) Strain energy   **(b)** Deformed shape

Fig. 10 Comparison between 2D first trial, 2D best fit and 3D Cauchy model for out-of-plane bias test

(a) Top view.   **(b)** Side view.

(c) Front view.   **(d)** Axonometric view.
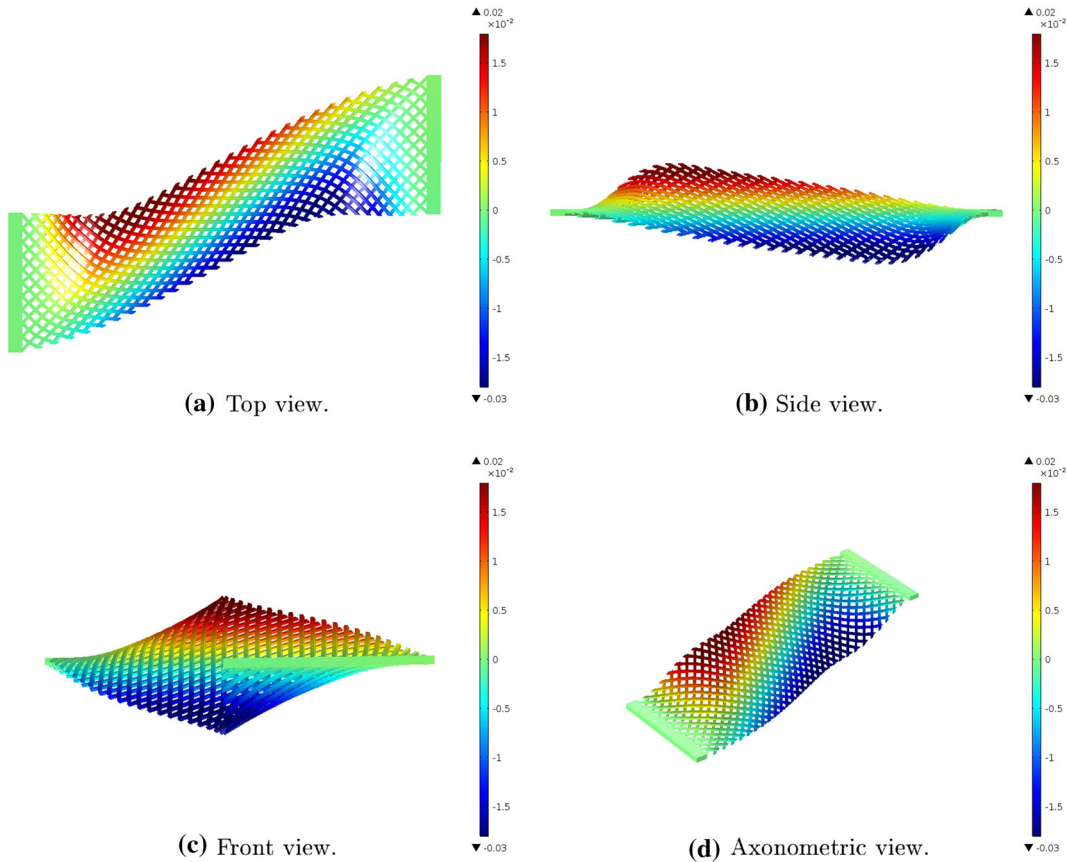
Fig. 11 Shear test. The legend refers to the out-of-plane displacement, u_3

This function is used, as in the previous case, to evaluate which set of stiffnesses is the best. We remark that the contribution produced by the deformed shape is averaged over the pivots' centers taken into consideration.

The results presented herein are the product of two iterative procedures aimed at the minimization of the objective functions defined in Eqs. (18) and (19). The Levenberg–Marquardt algorithm is employed to achieve this task.

In Fig. 8, the quantities used for the identification in the in-plane bias extension test are plotted for the 3D model and the 2D one (first trial, best fit). In each of the three plots in Fig. 8, it can be observed that the identification produced a good approximation of the objective curves concerning the micro-model.

Let us now consider the second experiment (out-of-plane bias shear test), where the set of constitutive parameters in Table 4 is used as first trial. Similarly to the previous case, we perform several simulations varying the corrective coefficients of K_t and K_n looking for the minimum value of Eq. (19), which is obtained using the final set of stiffnesses reported in Table 5. Before carrying out the iterations to achieve the results in Table 5, we verified that the second type of test was not influenced by the first three identified stiffnesses. This is clear looking at the plot in Fig. 9a, where it can be observed that the most relevant energy contributions are related to the last two material parameters to be identified. Further evidence of this fact is provided by the plot in Fig. 9b, which shows the axial placement of the line 2 indicated in Fig. 7 during the out-of-plane shear test (3D and 2D first trial) by using for the 2D model the first three identified stiffnesses. Clearly, this axial placement is independent of K_n and K_t.
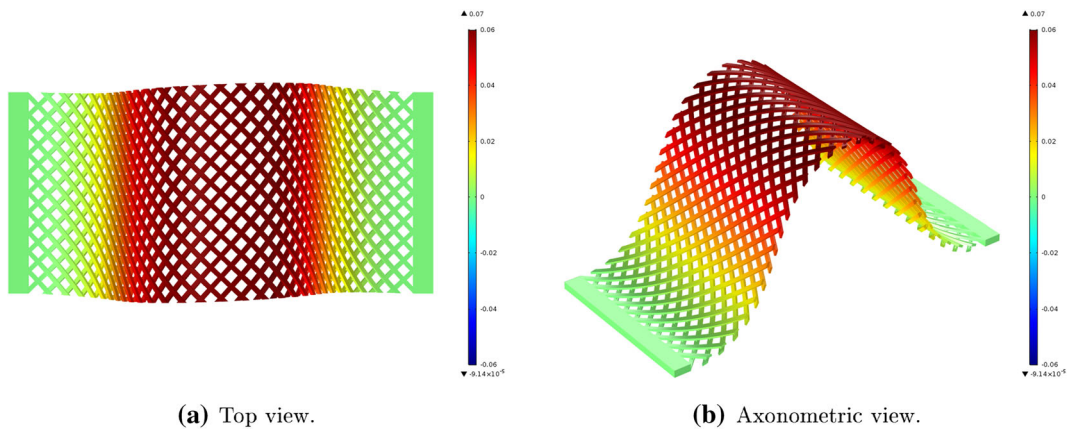

(a) Top view.

(b) Axonometric view.

Fig. 12 Compression test. The legend refers to the out-of-plane displacement, u_3

(a) Probe point P and Q for the micro-model.

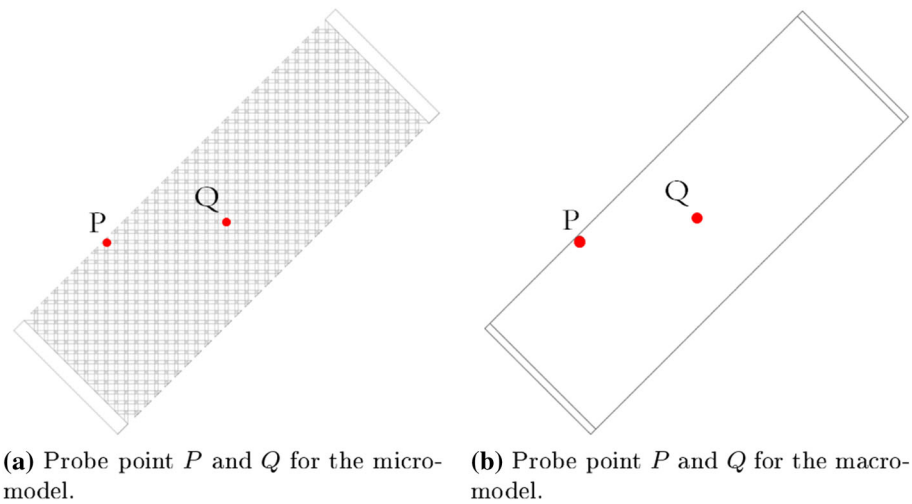**(b)** Probe point P and Q for the macro-model.

Fig. 13 In-plane shear test and compression test, evaluation points

In Fig. 10, the results of the fitting process for the out-of-plane bias shear test are shown. The plots report the comparison of the deformation energy and of the deformed shape between the macro-model and the micro-model.

4 Results of the identification process

In order to test the actual forecasting capability of the identified macro-model toward the 3D Cauchy model, we compare both in two other tests different from the ones used for the fitting. The view of 3D deformed shapes for both tests (see Figs. 11, 12) suggests referring to them as in-plane (even if buckling is observed, see [12,38,40]) shear test and in-plane (even if, also in this case, buckling is observed) compression test, respectively. The in-plane shear test prescribes the following boundary conditions: the short left side of the specimen is clamped, while the right short side is clamped and displaced rigidly upward (see Fig. 11a). The in-plane compression test prescribes the short left side to be fixed and a slider to be applied to the right one, with an inward uniform imposed displacement (see Fig. 12a).
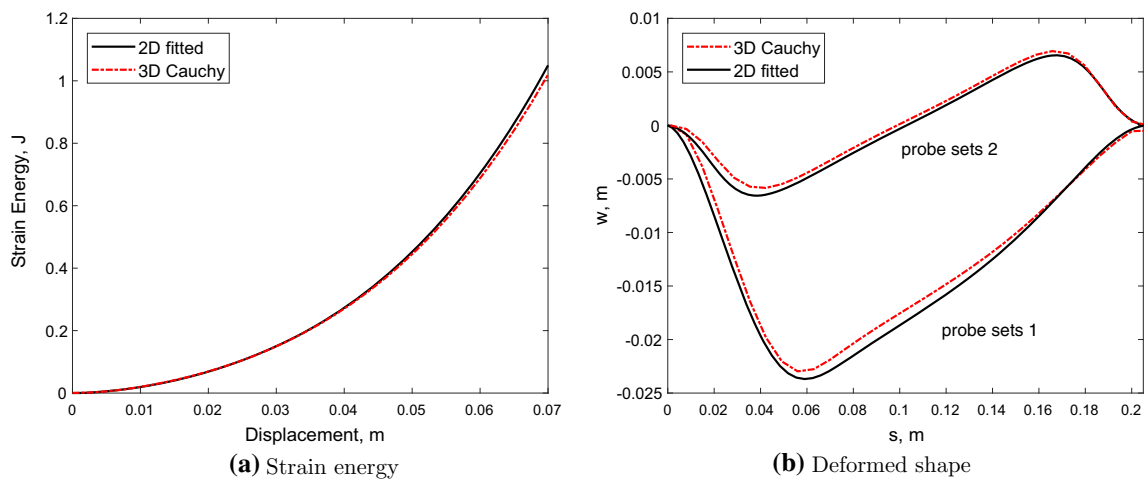

(a) Strain energy   **(b)** Deformed shape

Fig. 14 In-plane shear test, comparisons between micro-model and fitted macro-model
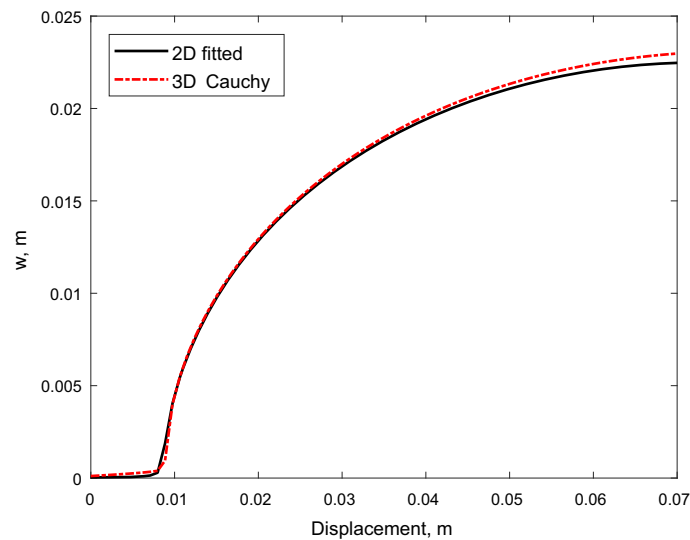
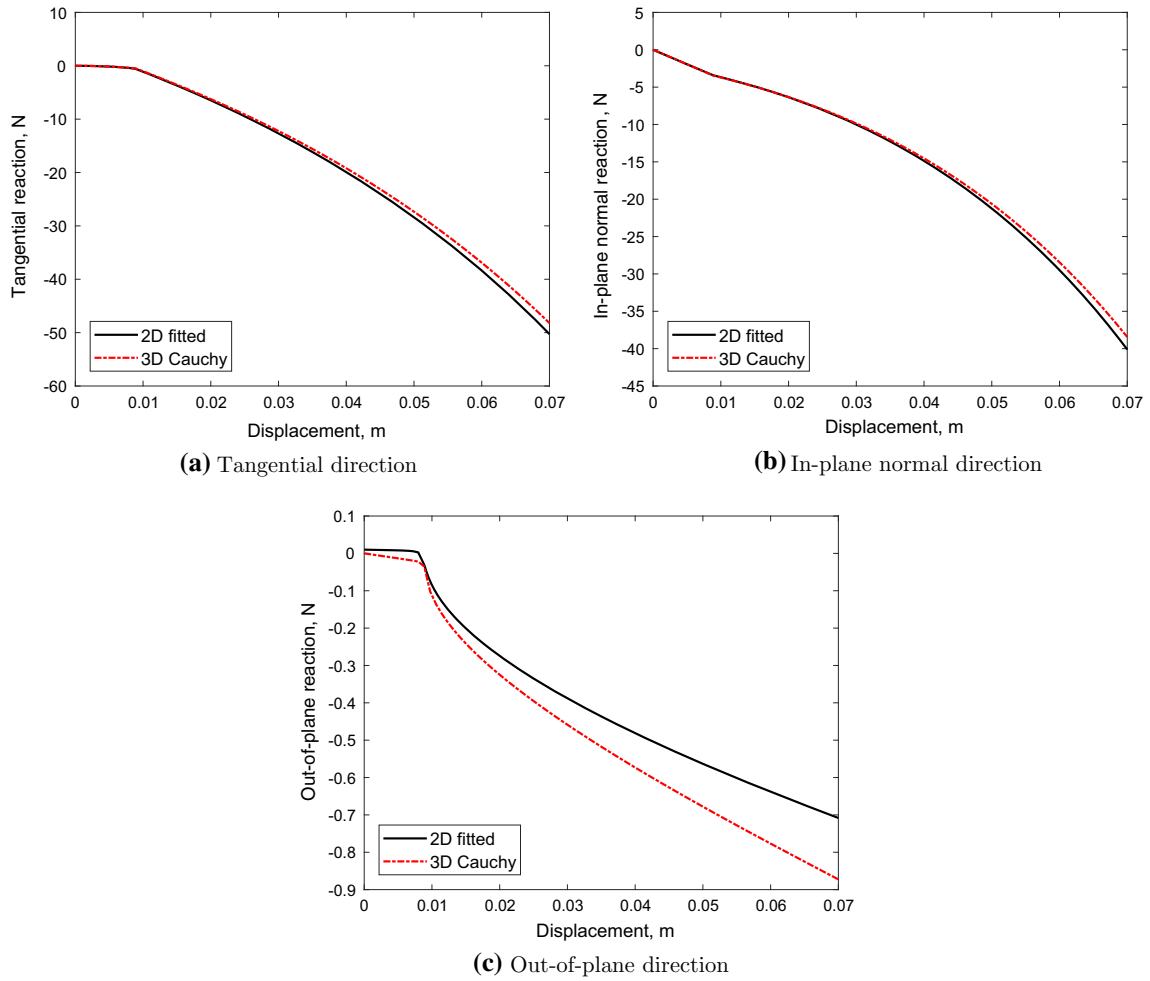**Fig. 15** In-plane shear test, out-of-plane displacement evaluated at point P

(a) Tangential direction

(b) In-plane normal direction

(c) Out-of-plane direction

Fig. 16 In-plane shear test, comparisons between micro- and macro-reaction forces
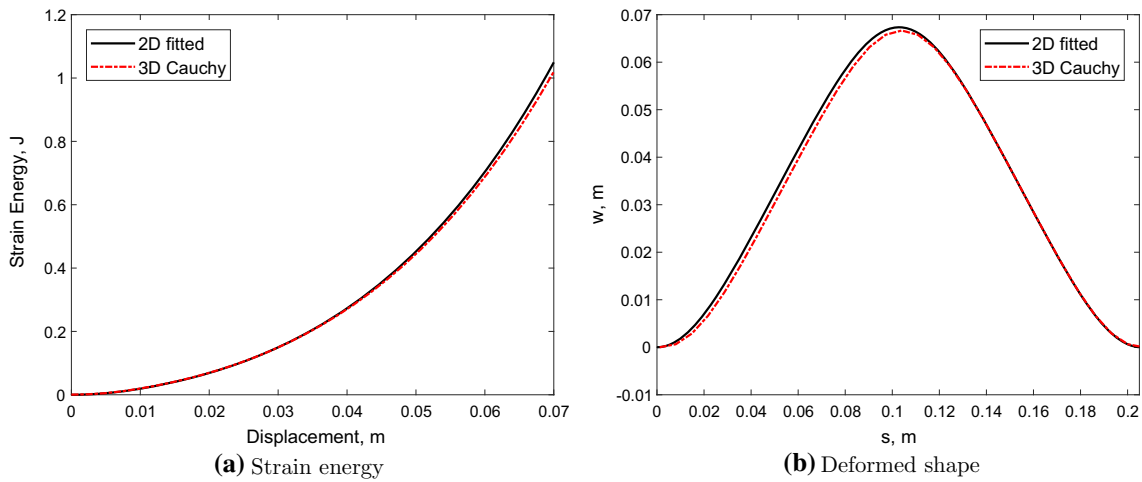

(a) Strain energy

(b) Deformed shape

Fig. 17 Compression test, comparisons between micro-model and fitted macro-model

Firstly, let us consider the in-plane shear test. As experimentally observed in [12], this type of test produces instability phenomena, which cause out-of-plane displacements of some regions of the specimen (see Fig. 11 where a numerical simulation is exhibiting this instability). The emergence of instability phenomena is both experimentally and numerically linked to the presence of defects. Experimentally, these defects can be geometrical (as in the numerics) or due to other factors (badly grasped specimen, asymmetry in the transmission of the load, internal imperfections of the specimen, etc.). Specifically, in the 3D model a small rotation has been assigned to the displaced side. Similarly, an imperfection has been assigned to the long sides of the homogenized model by applying a small force on the long sides, in correspondence of the points where the out-of-plane motion was expected.

By including such imperfections, it has been possible to obtain results allowing to perform the validation. For the validation, we compare some physical quantities: the total strain energy, the deformed shape (of the material lines in Fig. 7a, b), the reactions at the fixed edge and the out-of-plane displacement of one point P, which is at the vertex of the buckled region (see Fig. 13c, d). In Fig. 14a, the strain energy versus imposed displacement is plotted. The two curves are almost coincident, which means that the constitutive parameters introduced in the macro-model globally produce the same energy content, even in situations different from those used for their identification. Furthermore, the comparison between the deformed shapes in Fig. 14b displays small differences of few millimeters between the plotted curves for the probe points and lines labeled 1 and 2 in Fig. 7a, b.

Even more significant is the micro–macro-correspondence in Fig. 15, where the displacement of point P along the z axis is plotted. In Fig. 15, it is shown that the two models, in the in-plane shear test, are characterized by the same critical value of the displacement (after which buckling occurs). A further confirmation is provided by the plots of reaction forces in Fig. 16. We can observe that along the tangential and in-plane normal directions the agreement is very good between the curves, while along the out-of-plane direction there are some nonnegligible differences, despite having a similar trend. Such discrepancies might be a consequence of hypotheses lying at the basis of the reduced macro-model. Indeed, in the reduced description at macro-level, pivots' 'shearing' and 'bending' contributions —which are very likely to be relevant— have not been taken into account.

The second validation experiment gave similar results for all the quantities analyzed and discussed above. Indeed, the plots in Fig. 17a, b (strain energy and deformed shape of probe middle line) for the two models are almost overlapping. The out-of-plane displacement of a point Q (which reference position is shown in Fig. 13a, b, being at the vertex of the buckled shape in the current configuration) is reported in Fig. 18, while for reactions see Fig. 19. Considerations similar to those made for reactions shown in Fig. 16 can be made for Fig. 19.
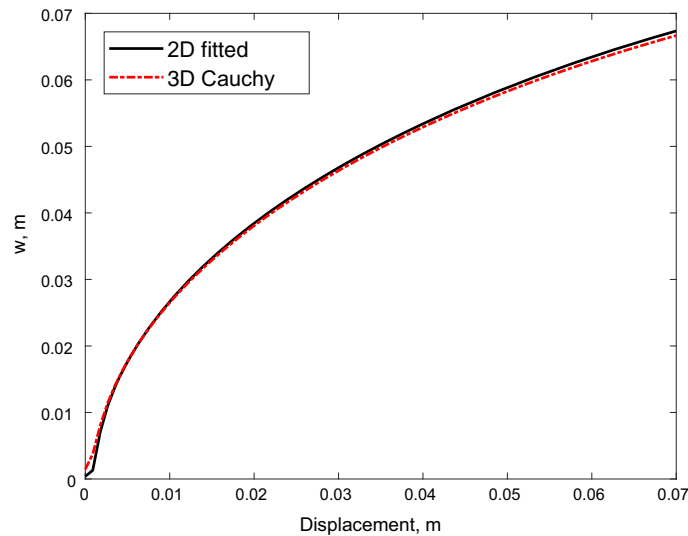

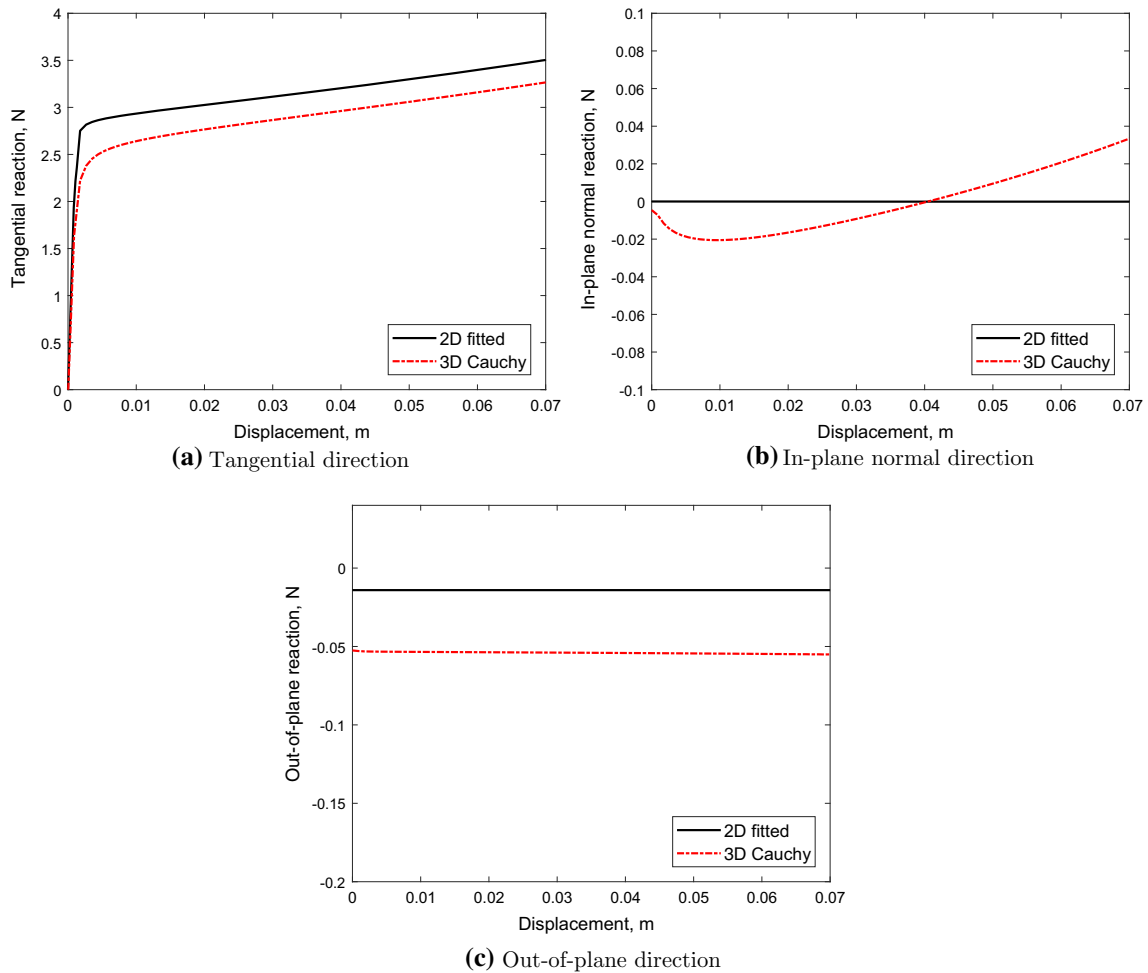**Fig. 18** Compression test, out-of-plane displacement evaluated at point Q

(a) Tangential direction

(b) In-plane normal direction

(c) Out-of-plane direction

Fig. 19 Compression test, comparisons between micro- and macro-reaction forces

5 Conclusions

The development of innovative new materials with specifically built microstructure requires predictive and efficient numerical models for properly simulating their mechanical behavior. While a 3D model is quite respectful of the first requirement, it is not likewise from the efficiency point of view. Until automatic calculus will not have a better capability of solving in a reasonable time the computationally complex equation systems required for the simulation of 3D models, reduced-order models will be necessary. In this paper, we dealt with an identification process of constitutive mechanical parameters of a homogenized 2D model with those of a 3D Cauchy pantographic structure. Differently from other cases, we considered also out-of-plane motions and strains. The work was divided in two steps with the aim of considering separately the energetic terms related to plane strains and out-of-plane ones. Firstly, we performed a plane bias extension test and we identified K_e, K_g and K_s. Then, by means of an out-of-plane bias shear test, we found K_n and K_t. Validation experiments have confirmed the goodness of the performed identification. It is remarkable that the results obtained for the in-plane shear test accurately reproduce the buckling response.

In appendix, a sensitivity study of the identified stiffnesses demonstrates that the identification carried out is consistent and, as far as possible, unambiguous. Furthermore, we note that the stiffness K_s related to the shear strain is the mechanical parameter characterizing prominently the response under uniaxial extension. As a matter of fact, a change in K_s implies the greatest differences on the objective function in Eq. (18).

A Appendix: Sensitivity of identified parameters

The identification process made possible to find a set of stiffnesses characterizing the mechanical behavior of the pantographic structure. The subsequent step of our investigation consists in estimating the sensitivity of the objective function upon changes in the constitutive parameters.

To this aim, further simulations were carried out using the macroscopic model. The values of identified stiffnesses were changed individually, and the results were compared with those obtained using such unchanged stiffnesses.

The in-plane bias extension test and the three stiffnesses K_e, K_g and K_s that characterize its mechanical behavior were initially considered. As mentioned before, in each simulation mechanical parameters were increased or decreased individually by $\pm 10\%$ and $\pm 20\%$. The outcome of such analysis is that there is one mechanical parameter which characterizes most the response under extension, that is, the stiffness K_s related to the shear strain. Indeed, it is possible to notice that a change in K_s produces the greatest differences on every contribution to the objective function in Eq. (18) (see Figs. 20b, 22b, 24b). In Figs. 21b, 23b and 25b, the relative differences of contributions to the objective function with respect to the unchanged identified stiffnesses are plotted.

In Fig. 22a–c, the angle θ is plotted varying the parameters K_e, K_s and K_g, respectively, in a neighborhood of the identified stiffnesses. In Fig. 23a–c, the relative difference for the angle θ is plotted varying, respectively, K_e, K_s and K_g. From this last figure, it can be observed that the relative difference of θ is comparable for similar relative changes in the stiffnesses K_e and K_s, while relative differences are much less when K_g changes.
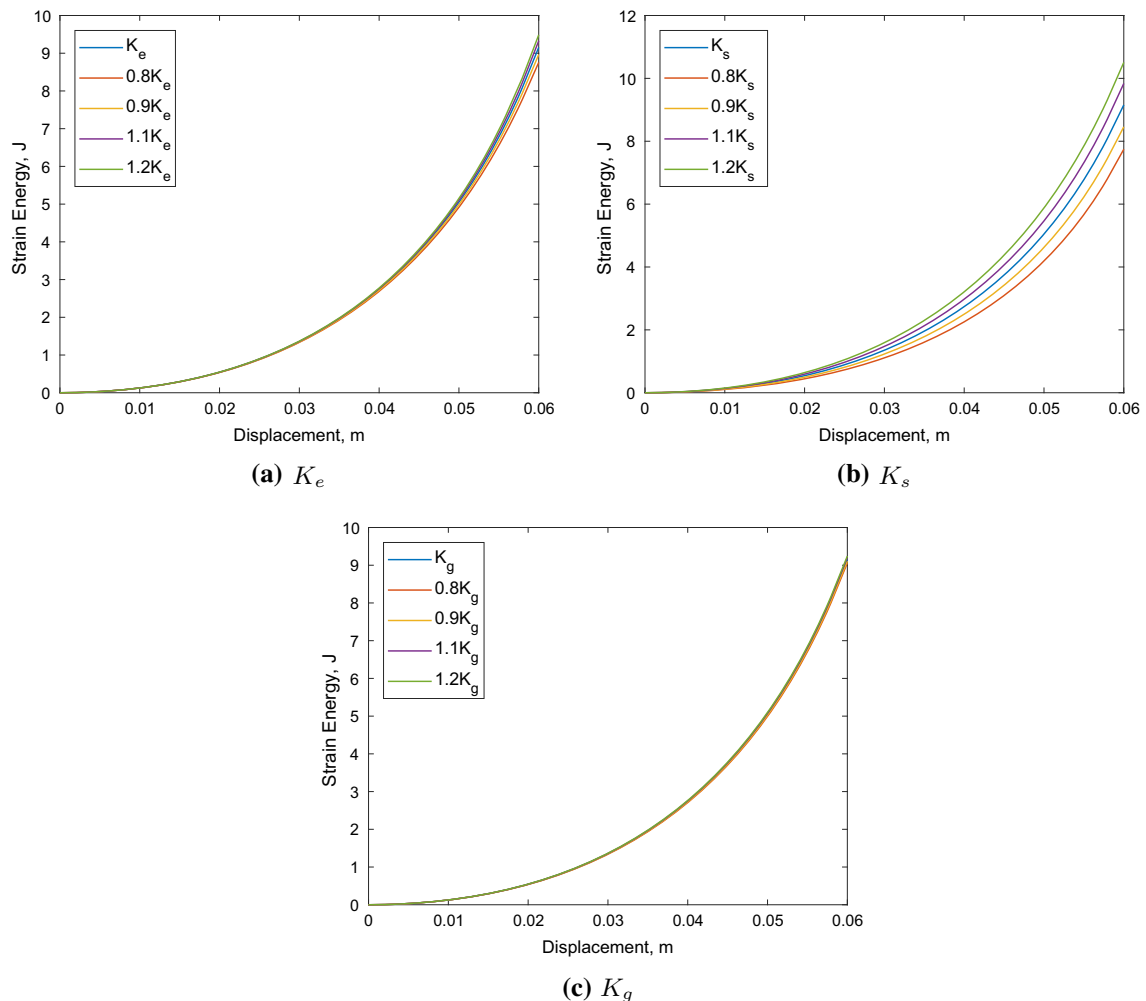

(a) K_e

(b) K_s

(c) K_g

Fig. 20 In-plane bias extension test, strain energy varying K_e, K_g and K_s

It is remarkable that the angle ϕ seems to depend on all the three stiffnesses in a similar way, as they produce comparable effects in each parametric study (see Figs. 24, 25).

Sensitivity analysis varying the constitutive stiffnesses has been carried out for the out-of-plane bias shear test too. As for the previous case, we want to evaluate the changes in the quantities involved in the objective function when K_n and K_t are varied of a certain amount. Also in this case, we consider relative changes of stiffnesses of $\pm 10\%$ and $\pm 20\%$. In Fig. 26, we observe that the magnitude of strain energy depends similarly both on K_n and on K_t. Furthermore, the sensitivity of the model is relevant for these two stiffnesses as shown by plots in Fig. 27. Indeed, relative changes of the stiffnesses, say of $X\%$, produce relative differences in the related quantities appearing in the objective function of about $X/2\%$.
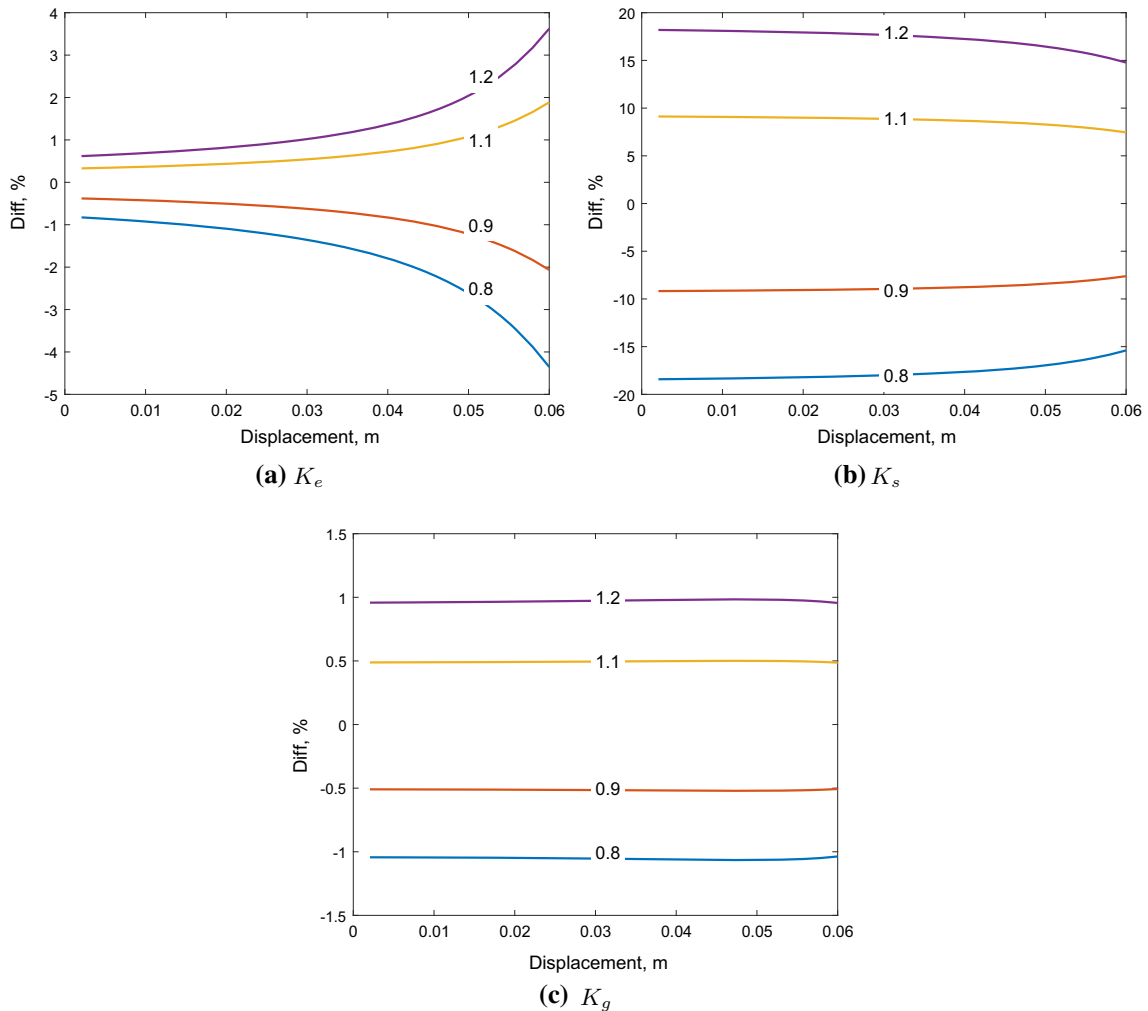

(a) K_e (b) K_s

(c) K_g

Fig. 21 In-plane bias extension test, relative changes in strain energy varying K_e, K_g and K_s

(a) K_e

(b) K_s

(c) K_g
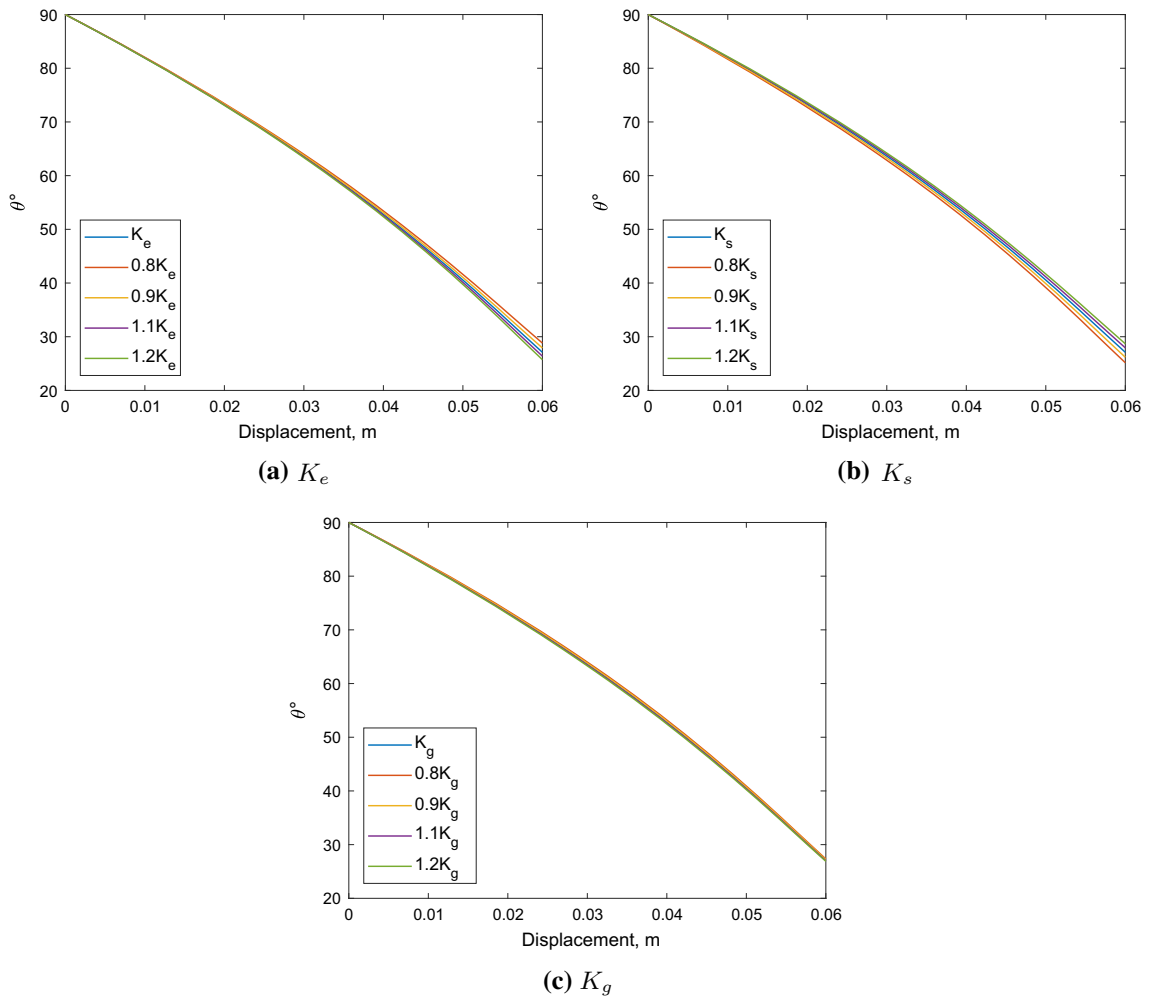
Fig. 22 In-plane bias extension test, values of the angle θ varying K_e, K_g and K_s

(a) K_e

(b) K_s

(c) K_g
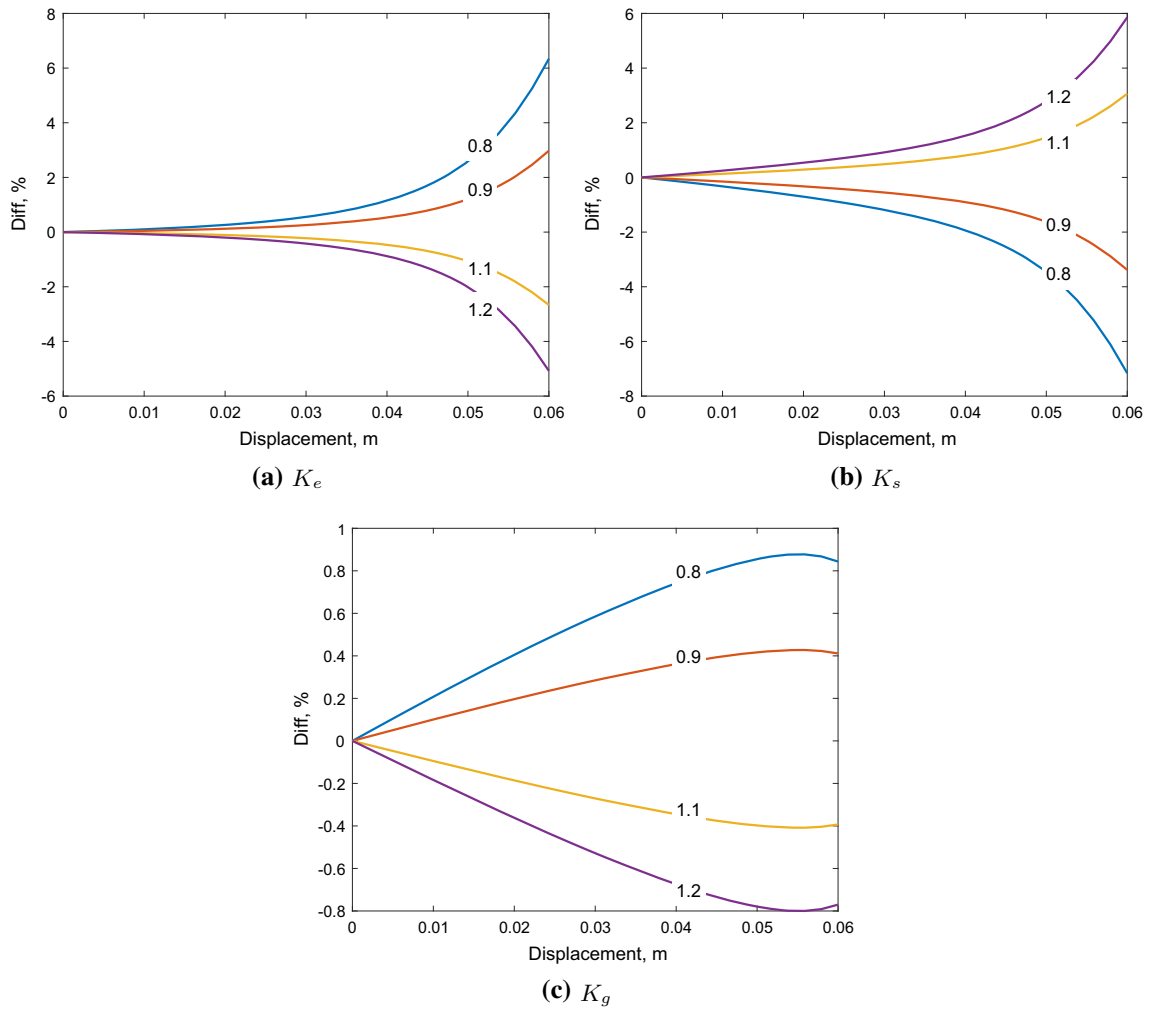
Fig. 23 In-plane bias extension test, relative changes in the angle θ varying K_e, K_g and K_s

(a) K_e

(b) K_s

(c) K_g
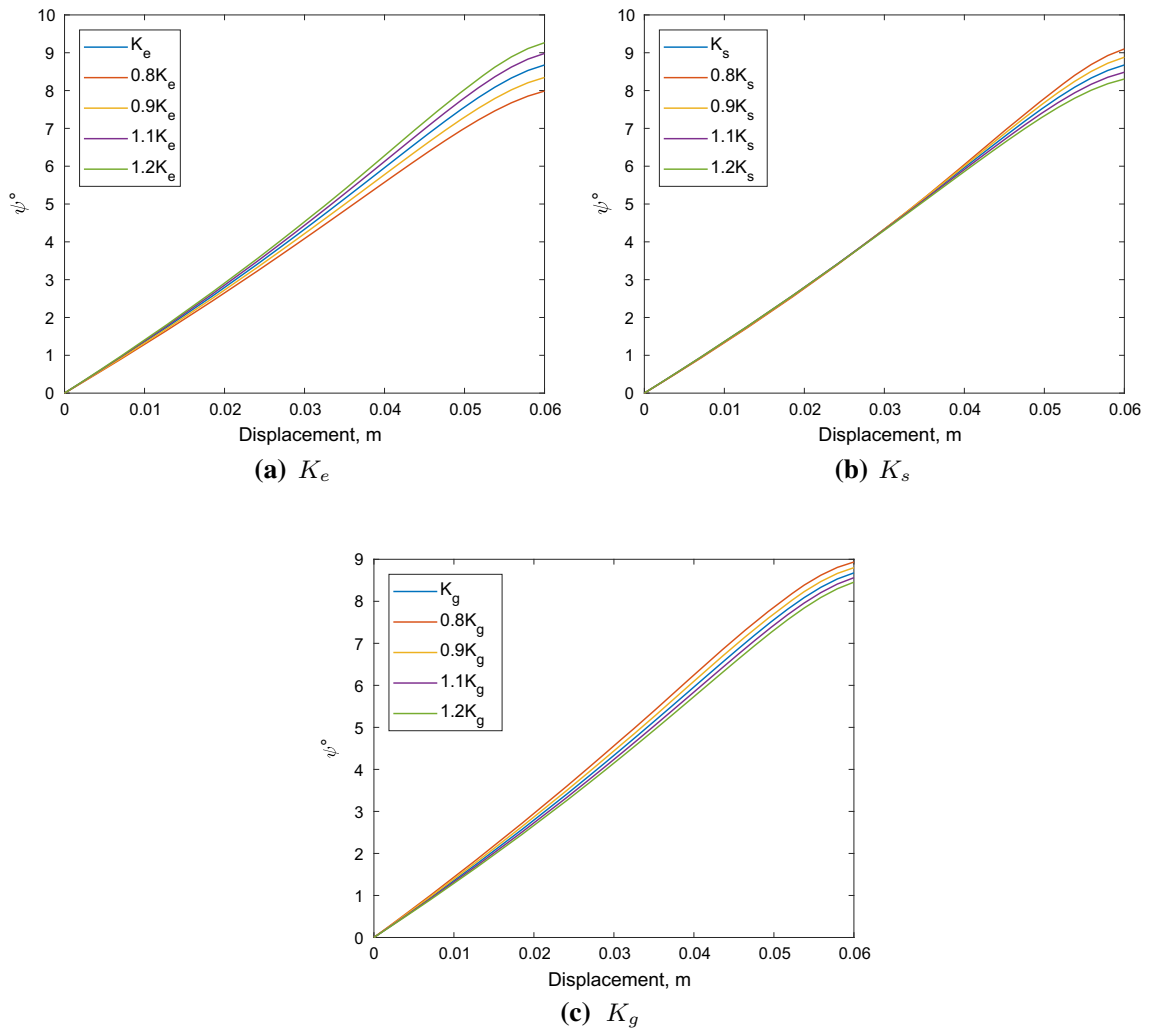
Fig. 24 In-plane bias extension test, values of the angle ψ varying K_e, K_g and K_s
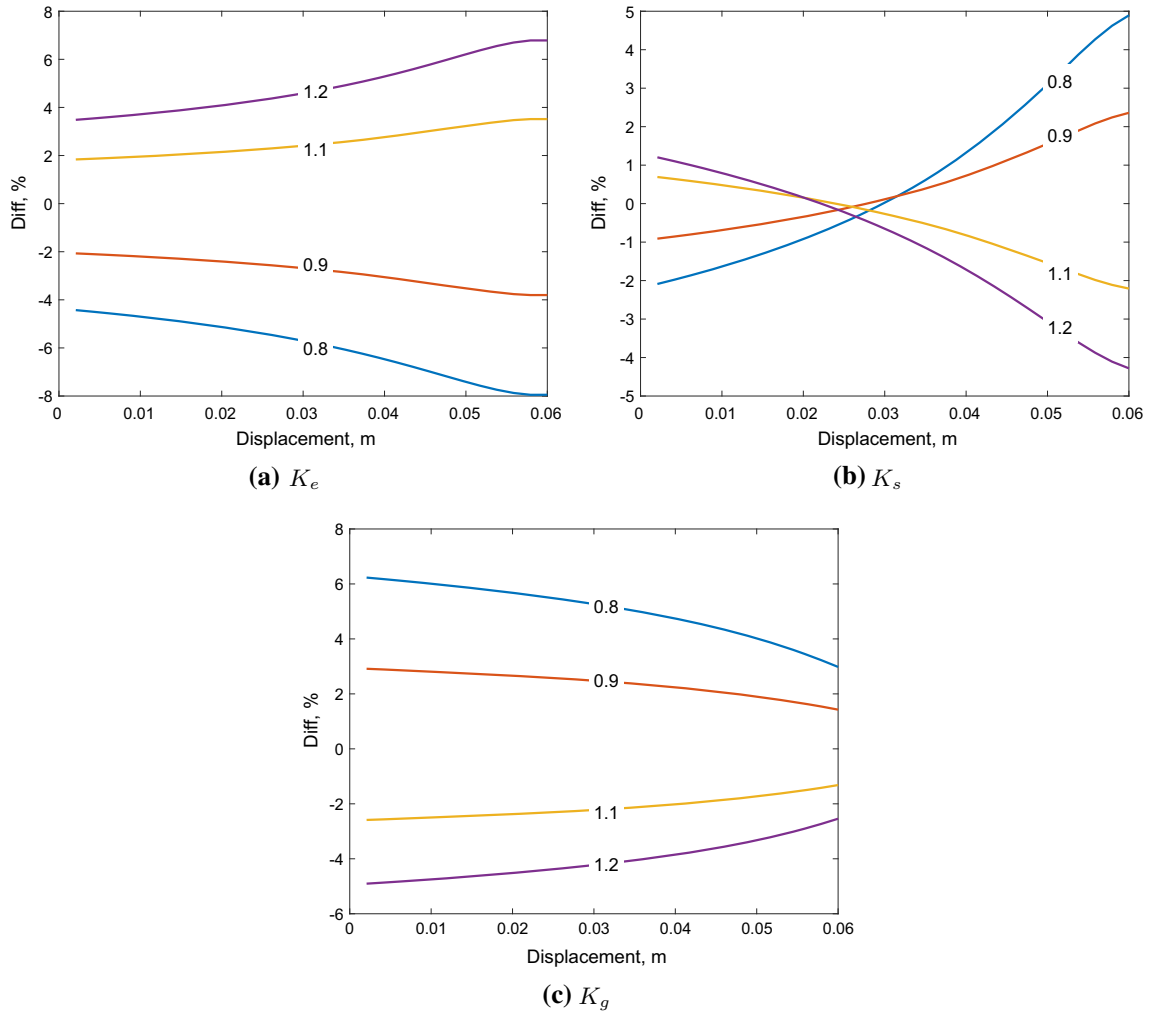
(a) K_e

(b) K_s

(c) K_g

Fig. 25 In-plane bias extension test, relative changes in the angle ϕ varying K_e, K_g and K_s
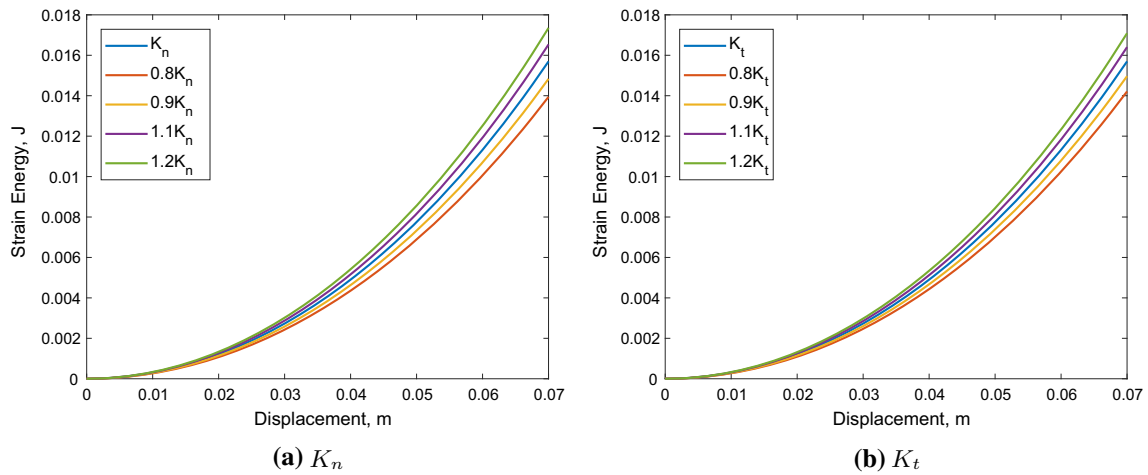
Fig. 26 Out-of-plane bias test, strain energy varying K_n and K_t
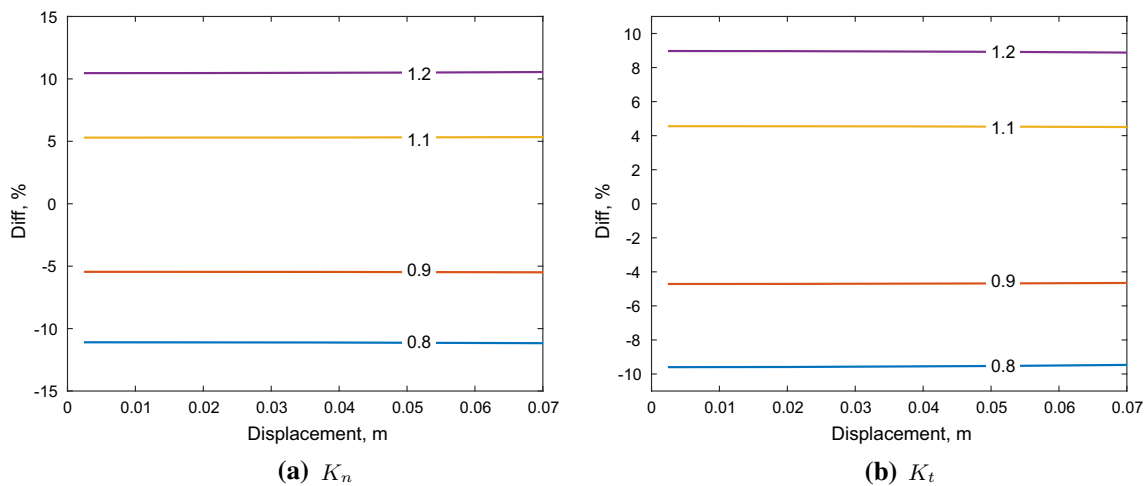

Fig. 27 Out-of-plane bias test, relative changes in strain energy varying K_n and K_t

References

1. Abali, B.E.: Computational Reality: Solving Nonlinear and Coupled Problems in Continuum Mechanics. Advanced Structured Materials, vol. 55. Springer, Berlin (2016)
2. Abali, B.E., Müller, W.H., dell'Isola, F.: Theory and computation of higher gradient elasticity theories based on action principles. Arch. Appl. Mech. **87**(9), 1495–1510 (2017)
3. Abali, B.E., Wu, C.-C., Müller, W.H.: An energy-based method to determine material constants in nonlinear rheology with applications. Contin. Mech. Thermodyn. **28**(5), 1221–1246 (2016)
4. Alibert, J., Corte, A.Della: Second-gradient continua as homogenized limit of pantographic microstructured plates: a rigorous proof. Z. Angew. Math. Phys. **66**(5), 2855–2870 (2015)
5. Alibert, J.-J., Seppecher, P., dell'Isola, F.: Truss modular beams with deformation energy depending on higher displacement gradients. Math. Mech. Solids **8**(1), 51–73 (2003)
6. Alsayednoor, J., Harrison, P.: Evaluating the performance of microstructure generation algorithms for 2-D foam-like representative volume elements. Mech. Mater. **98**, 44–58 (2016)
7. Alsayednoor, J., Harrison, P., Guo, Z.: Large strain compressive response of 2-D periodic representative volume element for random foam microstructures. Mech. Mater. **66**, 7–20 (2013)
8. Altenbach, H., Eremeyev, V.A.: Surface viscoelasticity and effective properties of materials and structures. In: Altenbach, H., Kruch, S. (eds.) Advanced Materials Modelling for Structures, vol. 19, pp. 9–16. Springer, Berlin (2013)

9. Andreaus, U., dell'Isola, F., Giorgio, I., Placidi, L., Lekszycki, T., Rizzi, N.L.: Numerical simulations of classical problems in two-dimensional (non) linear second gradient elasticity. Int. J. Eng. Sci. **108**, 34–50 (2016)

10. Andreaus, U., Spagnuolo, M., Lekszycki, T., Eugster, S.R.: A Ritz approach for the static analysis of planar pantographic structures modeled with nonlinear Euler-Bernoulli beams. Continu. Mech. Thermodyn. (2018). https://doi.org/10.1007/s00161-018-0665-3

11. Assidi, M., Boubaker, B.B., Ganghoffer, J.-F.: Equivalent properties of monolayer fabric from mesoscopic modelling strategies. Int. J. Solids Struct. **48**(20), 2920–2930 (2011)

12. Barchiesi, E., Ganzosch, G., Liebold, C., Placidi, L., Grygoruk, R., Müller, W.H.: Out-of-plane buckling of pantographic fabrics in displacement-controlled shear tests: experimental results and model validation. Contin. Mech. Thermodyn. (2018). https://doi.org/10.1007/s00161-018-0626-x

13. Barchiesi, E., Placidi, L.: A review on models for the 3D statics and 2D dynamics of pantographic fabrics. In: Sumbatyan, M. (ed.) Wave Dynamics and Composite Mechanics for Microstructured Materials and Metamaterials, vol. 59, pp. 239–258. Springer, Singapore (2017)

14. Barchiesi, E., Spagnuolo, M., Placidi, L.: Mechanical metamaterials: a state of the art. Math. Mech. Solids. (2018). https://doi.org/10.1177/1081286517735695

15. Battista, A., Cardillo, C., Del Vescovo, D., Rizzi, N.L., Turco, E.: Frequency shifts induced by large deformations in planar pantographic continua. Nanomech. Sci. Technol. Int. J. **6**(2), 161–178 (2015)

16. Boutin, C., dell'Isola, F., Giorgio, I., Placidi, L.: Linear pantographic sheets: asymptotic micro-macro models identification. Math. Mech. Complex Syst. **5**(2), 127–162 (2017)

17. Carinci, G., De Masi, A., Giardinà, C., Presutti, Errico: Hydrodynamic limit in a particle system with topological interactions. Arab. J. Math. **3**(4), 381–471 (2014)

18. Challamel, N., Kocsis, A., Wang, C.M.: Discrete and non-local elastica. Int. J. Non-Linear Mech. **77**, 128–140 (2015)

19. Chaouachi, F., Rahali, Y., Ganghoffer, J.-F.: A micromechanical model of woven structures accounting for yarn-yarn contact based on Hertz theory and energy minimization. Compos. Part B: Eng. **66**, 368–380 (2014)

20. Cuomo, M., dell'Isola, F., Greco, L.: Simplified analysis of a generalized bias test for fabrics with two families of inextensible fibres. Z. Angew. Math. Phys. **67**(3), 1–23 (2016)

21. De Masi, A., Merola, I., Presutti, E., Vignaud, Y.: Potts models in the continuum. Uniqueness and exponential decay in the restricted ensembles. J. Stat. Phys. **133**(2), 281–345 (2008)

22. Del Vescovo, D., Giorgio, I.: Dynamic problems for metamaterials: review of existing models and ideas for further research. Int. J. Eng. Sci. **80**, 153–172 (2014)

23. dell'Isola, F., Cuomo, M., Greco, L., Corte, A.Della: Bias extension test for pantographic sheets: numerical simulations based on second gradient shear energies. J. Eng. Math. **103**(1), 127–157 (2016)

24. dell'Isola, F., Corte, A.Della, Giorgio, I., Scerrato, D.: Pantographic 2D sheets: discussion of some numericalinvestigations and potential applications. Int. J. Non-Linear Mech. **80**, 200–208 (2016)

25. dell'Isola, F., Corte, A.Della, Greco, L., Luongo, A.: Plane bias extension test for a continuum with two inextensible families of fibers: a variational treatment with lagrange multipliers and a perturbation solution. Int. J. Solids Struct. **81**, 1–12 (2016)

26. dell'Isola, F., Giorgio, I., Pawlikowski, M., Rizzi, N.: Large deformations of planar extensible beams and pantographic lattices: heuristic homogenization, experimental and numerical examples of equilibrium. Proc. R. Soc. A **472**(2185), 23 (2016)

27. dell'Isola, F., Lekszycki, T., Pawlikowski, M., Grygoruk, R., Greco, L.: Designing a light fabric metamaterial being highly macroscopically tough under directional extension: first experimental evidence. Z. Angew. Math. Phys. **66**, 3473–3498 (2015)

28. dell'Isola, F., Seppecher, P., et al.: Pantographic metamaterials: an example of mathematically driven design and of its technological challenges. Contin. Mech. Thermodyn. (2018). https://doi.org/10.1007/s00161-018-0689-8

29. dell'Isola, F., Steigmann, D.J.: A two-dimensional gradient-elasticity theory for woven fabrics. J. Elast. **18**, 113–125 (2015)

30. Di Cosmo, F., Laudato, M., Spagnuolo, M.: Acoustic metamaterialsbased on local resonances: Homogenization, optimization andapplications. In: Altenbach, H., Pouget, J., Rousseau, M., Collet, B., Michelitsch, T. (eds.) Generalized Models and Non-classical Approaches in Complex Materials 1, vol. 89, pp. 247–274. Springer, Cham (2018)

31. Dos Reis, F., Ganghoffer, J.-F.: Discrete homogenization of architectured materials: implementation of the method in a simulation tool for the systematic prediction of their effective elastic properties. Tech. Mech. **30**(1–3), 85–109 (2010)

32. Dos Reis, F., Ganghoffer, J.-F.: Construction of micropolar continua from the asymptotic homogenization of beam lattices. Comput. Struct. **112**, 354–363 (2012)

33. Dos Reis, F., Ganghoffer, J.-F.: Homogenized elastoplastic response of repetitive 2D lattice truss materials. Comput. Mater. Sci. **84**, 145–155 (2014)

34. El Nady, K., Dos Reis, F., Ganghoffer, J.-F.: Computation of the homogenized nonlinear elastic response of 2D and 3D auxetic structures based on micropolar continuum models. Compos. Struct. **170**, 271–290 (2017)

35. Eremeyev, V.A., dell'Isola, F., Boutin, C., Steigmann, D.: Linear pantographic sheets: existence and uniqueness of weak solutions. J. Elast. **132**(2), 175–196 (2018)

36. Eremeyev, V.A., Pietraszkiewicz, W.: Material symmetry group and constitutive equations of micropolar anisotropic elastic solids. Math. Mech. Solids **21**(2), 210–221 (2016)

37. Franciosi, P., Spagnuolo, M., Salman, O.U.: Mean Green operators of deformable fiber networks embedded in a compliant matrix and property estimates. Contin. Mech. Thermodyn. (2018). https://doi.org/10.1007/s00161-018-0668-0

38. Ganzosch, G., dell'Isola, F., Turco, e, Lekszycki, T., Müller, W.H.: Shearing tests applied to pantographic structures. Acta Polytech. CTU Proc. **7**, 1–6 (2016)

39. Giorgio, I.: Numerical identification procedure between a micro-Cauchy model and a macro-second gradient model for planar pantographic structures. Z. Angew. Math. Phys. **67**(4), 1–17 (2016)

40. Giorgio, I., Corte, A.Della, dell'Isola, F., Steigmann, D.: Buckling modes in pantographic lattices. C. R. Mec. **344**(7), 487–501 (2016)

41. Giorgio, I., Harrison, P., dell'Isola, F., Alsayednoor, J., Turco, E.: Wrinkling in engineering fabrics: a comparison between two different comprehensive modelling approaches. Proc. R. Soc. A **474**(2216), 20 (2018)

42. Giorgio, I., Rizzi, N.L., Turco, E.: Continuum modelling of pantographic sheets for out-of-plane bifurcation and vibrational analysis. Proc. R. Soc. A **473**(2207), 21 (2017). https://doi.org/10.1098/rspa.2017.0636
43. Goda, I., Assidi, M., Ganghoffer, J.-F.: Equivalent mechanical properties of textile monolayers from discrete asymptotic homogenization. J. Mech. Phys. Solids **61**(12), 2537–2565 (2013)
44. Golaszewski, M., Grygoruk, R., Giorgio, I., Laudato, M., Di Cosmo, F.: Metamaterials with relative displacements in their microstructure: technological challenges in 3D printing, experiments and numerical predictions. Contin. Mech. Thermodyn. (2018). https://doi.org/10.1007/s00161-018-0692-0
45. Greco, L., Cuomo, M., Contrafatto, L.: A reconstructed local $\bar{B}$ formulation for isogeometric Kirchhoff-Love shells. Comput. Methods Appl. Mech. Eng. **332**, 462–487 (2018)
46. Greco, L., Giorgio, I., Battista, A.: In plane shear and bending for first gradient inextensible pantographic sheets: numerical study of deformed shapes and global constraint reactions. Math. Mech. Solids **22**(10), 1950–1975 (2017)
47. Guo, Z., Shi, X., Chen, Y., Chen, H., Peng, X., Harrison, P.: Mechanical modeling of incompressible particle-reinforced neo-Hookean composites based on numerical homogenization. Mech. Mater. **70**, 1–17 (2014)
48. Harrison, P.: Modelling the forming mechanics of engineering fabrics using a mutually constrained pantographic beam and membrane mesh. Compos. Part A Appl. Sci. Manuf. **81**, 145–157 (2016)
49. Harrison, P., Alvarez, M.F., Anderson, D.: Towards comprehensive characterisation and modelling of the forming and wrinkling mechanics of engineering fabrics. Int. J. Solids Struct. (2017). https://doi.org/10.1016/j.ijsolstr.2016.11.008
50. Khakalo, S., Balobanov, V., Niiranen, J.: Modelling size-dependent bending, buckling and vibrations of 2D triangular lattices by strain gradient elasticity models: applications to sandwich beams and auxetics. Int. J. Eng. Sci. **127**, 33–52 (2018)
51. Khakalo, S., Niiranen, J.: Form II of Mindlin's second strain gradient theory of elasticity with a simplification: for materials and structures from nano-to macro-scales. Eur. J. Mech. A Solids **71**, 292–319 (2018)
52. Laudato, M., Di Cosmo, F.: Euromech 579 Arpino 3–8 April 2017: Generalized and microstructured continua: new ideas in modeling and/or applications to structures with (nearly) inextensible fibers—a review of presentations and discussions. *Continu. Mech. Thermodyn.*https://doi.org/10.1007/s00161-018-0654-6 (2018)
53. Mandadapu, K.K., Abali, B.E., Papadopoulos, P.: On the polar nature and invariance properties of a thermomechanical theory for continuum-on-continuum homogenization. arXiv preprint arXiv:1808.02540 (2018)
54. Maurin, F., Greco, F., Desmet, W.: Isogeometric analysis for nonlinear planar pantographic lattice: discrete and continuum models. Contin. Mech. Thermodyn. (2018). https://doi.org/10.1007/s00161-018-0641-y
55. Milton, G., Briane, M., Harutyunyan, D.: On the possible effective elasticity tensors of 2-dimensional and 3-dimensional printed materials. Math. Mech. Complex Syst. **5**(1), 41–94 (2017)
56. Misra, A., Poorsolhjouy, P.: Identification of higher-order elastic constants for grain assemblies based upon granular micromechanics. Math. Mech. Complex Syst. **3**(3), 285–308 (2015)
57. Niiranen, J., Balobanov, V., Kiendl, J., Hosseini, S.B.: Variational formulations, model comparisons and numerical methods for Euler–Bernoulli micro-and nano-beam models. Math. Mech. Solids. (2017). https://doi.org/10.1177/1081286517739669
58. Placidi, L., Andreaus, U., Corte, A.Della, Lekszycki, T.: Gedanken experiments for the determination of two-dimensional linear second gradient elasticity coefficients. Z. Angew. Math. Phys. **66**(6), 3699–3725 (2015)
59. Placidi, L., Andreaus, U., Giorgio, I.: Identification of two-dimensional pantographic structure via a linear D4 orthotropic second gradient elastic model. J. Eng. Math. **103**(1), 1–21 (2017)
60. Placidi, L., El Dhaba, A.R.: Semi-inverse method à la Saint-Venant for two-dimensional linear isotropic homogeneous second-gradient elasticity. Math. Mech. Solids **22**(5), 919–937 (2017)
61. Placidi, L., Greco, L., Bucci, S., Turco, E., Rizzi, N.L.: A second gradient formulation for a 2D fabric sheet with inextensible fibres. Z. Angew. Math. Phys. **67**(5), 114 (2016)
62. Polizzotto, Castrenze: A second strain gradient elasticity theory with second velocity gradient inertia-Part I: constitutive equations and quasi-static behavior. Int. J. Solids Struct. **50**(24), 3749–3765 (2013)
63. Polizzotto, Castrenze: A second strain gradient elasticity theory with second velocity gradient inertia-Part II: dynamic behavior. Int. J. Solids Struct. **50**(24), 3766–3777 (2013)
64. Queiruga, A., Zohdi, T.: Microscale modeling of effective mechanical and electrical properties of textiles. Int. J. Numer. Methods Eng. **108**(13), 1603–1625 (2016)
65. Rahali, Y., Ganghoffer, J.-F., Chaouachi, F., Zghal, : Strain gradient continuum models for linear pantographic structures: a classification based on material symmetries. J. Geom. Symmetry Phys. **40**, 35–52 (2015)
66. Rahali, Y., Giorgio, I., Ganghoffer, J.F., dell'Isola, F.: Homogenization à la Piola produces second gradient continuum models for linear pantographic lattices. Int. J. Eng. Sci. **97**, 148–172 (2015)
67. Rahali, Y., Goda, I., Ganghoffer, J.-F.: Numerical identification of classical and nonclassical moduli of 3D woven textiles and analysis of scale effects. Compos. Struct. **135**, 122–139 (2016)
68. Saeb, S., Steinmann, P., Javili, A.: Aspects of computational homogenization at finite deformations: a unifying review from Reuss' to Voigt's bound. Appl. Mech. Rev. **68**(5), 050801 (2016)
69. Scerrato, D., Giorgio, I., Rizzi, N.: Three-dimensional instabilities of pantographic sheets with parabolic lattices: numerical investigations. Z. Angew. Math. Phys. **67**(3), 1–19 (2016)
70. Scerrato, D., Zhurba Eremeeva, I.A., Lekszycki, T., Rizzi, N.L.: On the effect of shear stiffness on the plane deformation of linear second gradient pantographic sheets. Z. Angew. Math. Mech.: ZAMM **96**(11), 1268–1279 (2016)
71. Shirani, M., Luo, C., Steigmann, D.J.: Cosserat elasticity of lattice shells with kinematically independent flexure and twist. Contin. Mech. Thermodyn. (2018). https://doi.org/10.1007/s00161-018-0679-x
72. Spagnuolo, M., Barcz, K., Pfaff, A., dell'Isola, F., Franciosi, P.: Qualitative pivot damage analysis in aluminum printed pantographic sheets: numerics and experiments. Mech. Res. Commun. **83**, 47–52 (2017)
73. Steigmann, D.J., dell'Isola, F.: Mechanical response of fabric sheets to three-dimensional bending, twisting, and stretching. Acta Mech. Sin. **31**(3), 373–382 (2015)
74. Turco, E., dell'Isola, F., Cazzani, A., Rizzi, N.L.: Hencky-type discrete model for pantographic structures: numerical comparison with second gradient continuum models. Z. Angew. Math. Phys. **67**, 28 (2016)

75. Turco, E., Giorgio, I., Misra, A., dell'Isola, F.: King post truss as a motif for internal structure of (meta) material with controlled elastic properties. R. Soc. Open Sci. **4**(10), 20 (2017)
76. Turco, E., Golaszewski, M., Giorgio, I., D'Annibale, F.: Pantographic lattices with non-orthogonal fibres: experiments and their numerical simulations. Compos. Part B Eng. **118**, 1–14 (2017)
77. Turco, E., Misra, A., Pawlikowski, M., dell'Isola, F., Hild, F.: Enhanced Piola-Hencky discrete models for pantographic sheets with pivots without deformation energy: numerics and experiments. Int. J. Solids Struct. **147**, 94–109 (2018)
78. Turco, E., Rizzi, N.L.: Pantographic structures presenting statistically distributed defects: numerical investigations of the effects on deformation fields. Mech. Res. Commun. **77**, 65–69 (2016)
79. Yang, H., Ganzosch, G., Giorgio, I., Abali, B.E.: Material characterization and computations of a polymeric metamaterial with a pantographic substructure. Z. Angew. Math. Phys. **69**(4), 16 (2018)